

A comprehensive analysis of air-sea CO₂ flux uncertainties constructed from surface ocean data products

Daniel J Ford¹, Josh Blannin², Jennifer Watts³, Andrew Watson¹, Peter Landschützer⁴, Annika Jersild⁵, and Jamie Shutler¹

¹University of Exeter

²Met Office

³University of Exeter Cornwall Campus

⁴Flanders Marine Institute

⁵Max Planck Institute for Meteorology

April 01, 2024

Abstract

Increasing anthropogenic CO₂ emissions to the atmosphere are partially sequestered into the global oceans through the air-sea exchange of CO₂ and its subsequent movement to depth, and this collective large-scale absorption is commonly referred to as the global ocean carbon sink. Quantifying this ocean carbon sink provides a key component for closing the global carbon budget which is used to inform and guide policy decisions. These estimates are typically accompanied by an uncertainty budget built by selecting what are perceived as critical uncertainty components based on selective experimentation. However, there is a growing realisation that these budgets are incomplete and may be underestimated, which limits their power as a constraint within global budgets. In this study, we present a methodology for quantifying spatially and temporally varying uncertainties in the air-sea CO₂ flux calculations and data that allows an exhaustive assessment of all known sources of uncertainties, including decorrelation length scales between gridded measurements, and the approach follows standard uncertainty propagation methodologies. The resulting standard uncertainties are higher than previously suggested budgets, but the components are consistent with previous work, and they identify how the significance and importance of key uncertainty components change in space and time. For an exemplar method (the UEP-FNN-U method) the work identifies that we can currently estimate the annual ocean carbon sink to an accuracy of $\pm 0.72 \text{PgCyr}^{-1}$ (1 standard deviation uncertainty). Due to this method having been built on established uncertainty propagation and approaches, it appears applicable to all data-product assessments of the ocean carbon sink.

Hosted file

Ford_et_al_OceanICU_neural_framework_manuscript.docx available at <https://authorea.com/users/563449/articles/737255-a-comprehensive-analysis-of-air-sea-co2-flux-uncertainties-constructed-from-surface-ocean-data-products>

Hosted file

Ford_et_al_OceanICU_neural_framework_supportinginformation_temp.docx available at <https://authorea.com/users/563449/articles/737255-a-comprehensive-analysis-of-air-sea-co2-flux-uncertainties-constructed-from-surface-ocean-data-products>

A comprehensive analysis of air-sea CO₂ flux uncertainties constructed from surface ocean data products

Daniel J. Ford¹, Josh Blannin^{1,a}, Jennifer Watts¹, Andrew J. Watson², Peter Landschützer³, Annika Jersild^{4,b} and Jamie D. Shutler¹

¹ Department of Earth and Environmental Science, University of Exeter, Cornwall, TR10 9EZ, UK

² Global Systems Institute, University of Exeter, Devon, EX4 4RJ, UK

³ Flanders Marine Institute (VLIZ), Jacobsenstraat 1, 8400 Ostend, Belgium

⁴ Max Planck Institute for Meteorology, Hamburg, Germany

^a now at: Met Office, Exeter, EX1 3PB, UK

^b now at: Global Modelling and Assimilation Office (GMAO), NASA Goddard Space Flight Center, Greenbelt, MD, USA / Earth System Science Interdisciplinary Center, University of Maryland, College Park, MD, USA

Corresponding author: Daniel J. Ford (d.ford@exeter.ac.uk)

Abstract

Increasing anthropogenic CO₂ emissions to the atmosphere are partially sequestered into the global oceans through the air-sea exchange of CO₂ and its subsequent movement to depth, and this collective large-scale absorption is commonly referred to as the global ocean carbon sink. Quantifying this ocean carbon sink provides a key component for closing the global carbon budget which is used to inform and guide policy decisions. These estimates are typically accompanied by an uncertainty budget built by selecting what are perceived as critical uncertainty components based on selective experimentation. However, there is a growing realisation that these budgets are incomplete and may be underestimated, which limits their power as a constraint within global budgets. In this study, we present a methodology for quantifying spatially and temporally varying uncertainties in the air-sea CO₂ flux calculations and data that allows an exhaustive assessment of all known sources of uncertainties, including decorrelation length scales between gridded measurements, and the approach follows standard uncertainty propagation methodologies. The resulting standard uncertainties are higher than previously suggested budgets, but the components are consistent with previous work, and they identify how the significance and importance of key uncertainty components change in space and time. For an exemplar method (the UEP-FNN-U method) the work identifies that we can currently estimate the annual ocean carbon sink to an accuracy of $\pm 0.72 \text{ Pg C yr}^{-1}$ (1 standard deviation uncertainty). Due to this method having been built on established uncertainty propagation and

35 approaches, it appears applicable to all data-product assessments of the ocean carbon sink.

36

37 **Highlights**

- 38 1. A framework to calculate standard uncertainty budgets for air-sea CO₂ flux data that considers all
39 known sources of uncertainty is described.
- 40 2. Spatially and temporally varying air-sea CO₂ flux uncertainties including their spatial
41 decorrelation lengths are calculated.
- 42 3. For an exemplar data-product based estimate of the global ocean carbon sink we identify a 1 σ
43 uncertainty of ± 0.72 Pg C yr⁻¹.

44

45 **1. Introduction**

46 Anthropogenic carbon dioxide (CO₂) emissions are continuing to increase and since the 1800s the
47 ocean has acted as a natural CO₂ sink helping to slow the rise in atmospheric CO₂ and the resultant
48 global heating. This uptake equates to ~25 % of all anthropogenic CO₂ emissions and is occurring at
49 an increasing rate reaching ~2.9 petagrams of carbon per year (Pg C yr⁻¹; 1 Pg C = 10¹⁵ grams of
50 carbon) in recent years (Friedlingstein et al., 2023). Our ability to quantify and resolve the annual
51 uptake of CO₂ by the global oceans currently comes from two sources; (1) observation data-product
52 based assessments that extrapolate and combine sparse ocean CO₂ observations with satellite and re-
53 analysis data into global fields through time and (2) analyses from complex global biogeochemical
54 models. Along with globally complete datasets, the data-product based assessments also rely on
55 sparse in situ observations of the fugacity of CO₂ in seawater (fCO₂(_{sw})) which are collated into the
56 annual releases of the Surface Ocean CO₂ Atlas (SOCAT) (Bakker et al., 2016). In many of these data-
57 product based approaches, these in situ data are matched to variables such as satellite, reanalysis and
58 model-based data of sea surface temperature (SST), salinity (SSS), mixed layer depth (MLD) and
59 chlorophyll-a (Chau et al., 2022; Gregor & Gruber, 2021; Iida et al., 2021; Landschützer et al., 2014;
60 Watson et al., 2020), which are used to describe the physical, biological and chemically driven
61 variability in fCO₂(_{sw}) (Shutler et al., 2024). The relationships between these variables and fCO₂(_{sw})
62 are then estimated within predefined provinces or biogeochemical regions (e.g., using multi linear
63 regressions, neural network or other machine learning techniques) to allow globally complete fCO₂(_{sw})
64 fields through time to be produced (Chau et al., 2022; Gregor & Gruber, 2021; Iida et al., 2021;
65 Landschützer et al., 2016; Watson et al., 2020). These complete fields are then combined with a host
66 of data including more satellite observations, model and re-analysis datasets to calculate the air-sea
67 CO₂ fluxes, and then integrated into global or regional annual budgets (as described within Shutler et
68 al., 2024 and used by most of the data-product based ocean sink estimates within Friedlingstein et
69 al., 2023; and the six methods in Fay et al., 2021).

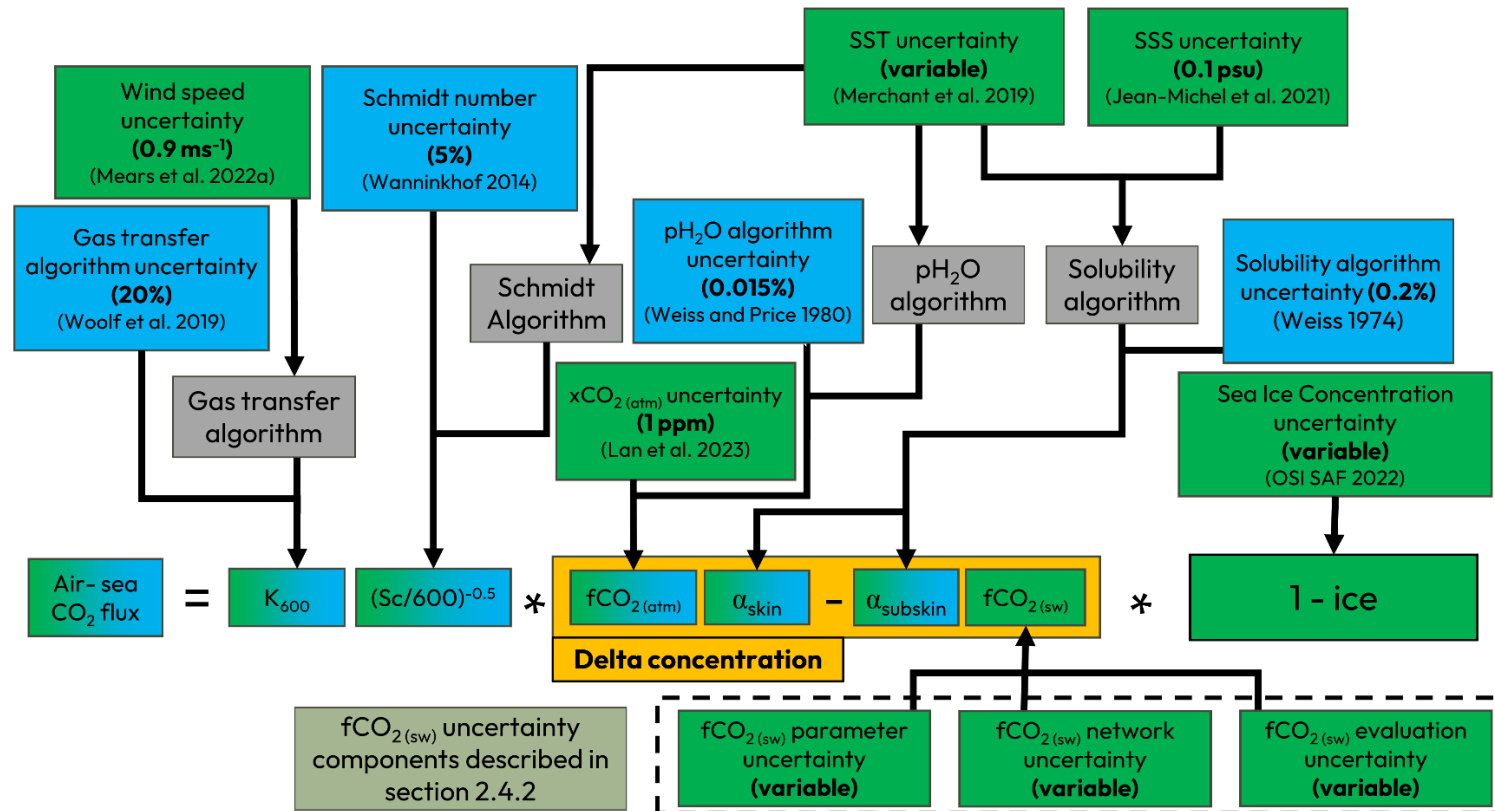
70 The current uncertainty characterisation on the resulting air-sea fluxes and the integrated net sink
71 estimates from these outputs are largely based on a single estimates that are assumed constant in space
72 or time. For example, Landschützer et al. (2014) estimate an uncertainty of $\sim 0.53 \text{ Pg C yr}^{-1}$ for one
73 data-product based assessment which comprised three sources of uncertainty, though dominated
74 mainly by one empirical parameterisation used within the calculation (the gas transfer
75 parameterisation, which was assessed to contribute to $\sim 0.4 \text{ Pg C yr}^{-1}$ of the uncertainty budget).
76 Within the Global Carbon Budget (GCB) (Friedlingstein et al., 2023) uncertainties on all data-product
77 ocean carbon sink assessments are estimated (as 1 standard deviation, 1σ) using literature values for a
78 selection of uncertainty sources including the standard deviation of the seven data product ensemble
79 in the GCB (contributing 0.3 Pg C yr^{-1}), the $f\text{CO}_2_{(\text{sw})}$ mapping (contributing 0.2 Pg C yr^{-1} to the
80 uncertainty budget) from Landschützer et al. (2014), the gas transfer coefficient (0.2 Pg C yr^{-1}) from
81 Ho et al. (2011) and Wanninkhof et al. (2013), the wind speed data input (0.1 Pg C yr^{-1}) from Fay et
82 al. (2021), the in situ $f\text{CO}_2_{(\text{sw})}$ observation uncertainty (0.2 Pg C yr^{-1}) from Wanninkhof et al. (2013)
83 and a land to ocean river flux adjustment (0.3 Pg C yr^{-1} which unlike the other components is the 2σ
84 value) due to natural CO_2 outgassed due to riverine material from Regnier et al. (2022). These
85 components are assumed spatially and temporally independent (i.e. uncorrelated), resulting in a fixed
86 annual standard 1σ uncertainty of $\pm 0.6 \text{ Pg C yr}^{-1}$. Whilst a good first step and pragmatic solution, this
87 approach does not systematically identify and characterise all sources of uncertainty and largely
88 overlooks spatial correlation which is important for some variables critical in the calculation (Watson
89 et al., 2009). Because of this, it is likely that these estimates of the uncertainties may be
90 underestimated, whilst many will vary through both space and time dependent upon data coverage
91 (Hauck, Nissen, et al., 2023) and environmental conditions. Furthermore, the apparent gradual
92 divergence that has been observed between the model and data-product based assessments within the
93 GCB assessments (Friedlingstein et al., 2022, 2023) may be, in part, driven by, or at least confused by,
94 unconstrained or incomplete uncertainty budgets. Jersild and Landschützer (2024) provide spatially
95 and temporally explicit uncertainties for some components of the air-sea CO_2 flux but do not
96 systematically evaluate all known sources of uncertainty and their approach is not simply applicable
97 to all data-products within the GCB. Clearly, a full uncertainty budget for both the model and data-
98 product based estimates is needed to support any conclusions as to which estimate is the more
99 credible. Similarly, a more complete standard uncertainty budget would guide where to focus efforts
100 towards reducing these uncertainties and improving the quantification of the global ocean CO_2 sink.

101 These complexities identify a desire for spatially and temporally varying uncertainties where all
102 known sources of uncertainty are systematically evaluated into a full standard uncertainty budget.
103 Established frameworks and methods for assessing uncertainty components exist which can be used to
104 build standard uncertainty budgets (BIPM, 2008) which were originally developed by the metrology
105 community, but have since seen widespread application in other scientific realms including ocean

106 satellite remote sensing and in situ studies (e.g., Banks et al., 2020; Dong et al., 2021) and these use
107 standard uncertainty propagation techniques (Taylor, 1997).

108 Within this study, we present a complete spatially and temporally varying air-sea CO₂ flux uncertainty
109 budget which systematically assesses all known sources of uncertainty and propagates these using
110 standard techniques (Taylor, 1997). To complement the baseline air-sea CO₂ flux uncertainty budget,
111 we also develop an approach to estimate spatially and temporally complete fCO_{2(sw)} uncertainties for
112 an exemplar feed forward neural network interpolation approach, that considers multiple sources of
113 uncertainty. We highlight how the uncertainty approach for the interpolated fields can be adapted to
114 other data-product based approaches which use different fCO_{2(sw)} interpolation methods. The resulting
115 air-sea CO₂ flux uncertainties are then globally integrated to produce a global time varying
116 uncertainty budget for the net air-sea CO₂ flux, or ocean CO₂ sink, and the dominant components
117 within this uncertainty budget are assessed. These results are discussed in the context of the GCB
118 global ocean CO₂ sink uncertainty estimates but the methods can also be applied regionally. The
119 uncertainty approach for the complete air-sea CO₂ fluxes and the integrated net sink values are
120 applicable to any data based approach.

121



122

123 **Figure 1:** Flowchart indicating the sources of uncertainty that contribute to each term in the air-sea CO₂ flux calculation described in section 2.2 and
 124 integrated in section 2.5. Green boxes indicate a component that decorrelates over a spatial and temporal scale, blue boxes indicate globally correlated
 125 components and grey boxes indicate functions for which uncertainties are propagated through using a Monte Carlo approach. The $f\text{CO}_2(\text{sw})$ uncertainty
 126 components (grouped by the dashed line box) are described in section 2.4.2. References within the flowchart are for the gas transfer algorithm uncertainty
 127 (Woolf et al., 2019), wind speed uncertainty (Mears et al., 2022a), Schmidt number algorithm uncertainty (Wanninkhof, 2014), partial pressure of water
 128 vapour (pH_2O) algorithm (Weiss & Price, 1980), $x\text{CO}_2(\text{atm})$ uncertainty (Lan et al., 2023), SST uncertainty (Merchant et al., 2019), SSS uncertainty (Jean-
 129 Michel et al., 2021), solubility algorithm uncertainty (Weiss, 1974) and the sea ice concentration uncertainty (OSI SAF, 2022). Acronyms in flowchart are gas
 130 transfer coefficient (K_{600}), Schmidt number (Sc), fugacity of CO₂ in atmosphere ($f\text{CO}_2(\text{atm})$) and seawater ($f\text{CO}_2(\text{sw})$) and solubility at the subskin (α_{subskin}) and
 131 skin (α_{skin}).

132 2. Methods

133 2.1. Input datasets

134 In situ monthly 1 degree gridded SOCAT2023 $fCO_2_{(sw)}$ observations which have been reanalysed to
 135 the depth consistent temperature CCI-SST v2.1 (Merchant et al., 2019) dataset were downloaded from
 136 Ford et al. (2023). Data were extracted for the period 1985 to 2022. Following the recommendations
 137 of Shutler et al. (2024) all satellite or re-analysis data choices focussed on climate data to ensure long-
 138 term data stability and the availability of uncertainty data. Satellite or reanalysis datasets were
 139 retrieved from their respective sources at their native temporal and spatial resolution (see
 140 Supplementary Table S1 for all the datasets used within this study) and averaged (mean) to the same
 141 monthly 1 degree global grid as the SOCAT observations. Some datasets did not cover the full
 142 temporal period and these periods were filled with a 10 year climatological monthly mean from the
 143 respective end of the timeseries (i.e if missing data occurred at the start of the timeseries, a 10 year
 144 monthly climatology from the start of the available data was constructed). Anomalies for each
 145 variable were calculated with respect to a monthly climatology between 1985 and 2022. The GCB
 146 (Friedlingstein et al., 2023) version of the UoEx-Watson product was retrieved from Hauck,
 147 Landschützer et al. (2023).

148 The CCI-SST and EUMETSAT Ocean and Sea Ice Satellite Application Facility (OSISAF) sea ice
 149 concentrations were retrieved with a daily coincident uncertainty field. The uncertainties within these
 150 data are correlated spatially to around 100-300 km and 3 days temporally (Kern, 2021), and therefore
 151 we assumed the uncertainties are correlated within these scales when producing the monthly 1 degree
 152 uncertainties.

153

154 2.2. Air-sea CO₂ fluxes

155 The air-sea CO₂ flux calculations were carried out using the open source FluxEngine toolbox
 156 (Holding et al., 2019; Shutler et al., 2016), which provides traceable, consistent, and configurable air-
 157 sea CO₂ flux calculations. The air-sea CO₂ flux (F) can be expressed in a bulk parameterisation as:

$$158 \quad F = K_{600} \left(\frac{Sc}{600} \right)^{-0.5} \left(\alpha_{subskin} fCO_2_{(sw,subskin)} - \alpha_{skin} fCO_2_{(atm)} \right) (1 - ice) \quad (1)$$

159 Which is consistent with the rapid model of Woolf et al., (2016) and where K_{600} is the gas transfer
 160 coefficient estimated using the Nightingale et al. (2000) parameterisation and wind speeds from the
 161 Cross Calibrated Multi-Platform dataset (CCMP; v3.1) (Mears et al., 2022a, 2022b). Sc is the Schmidt
 162 number estimated using the calculation in Wanninkhof et al. (2014) and the ocean's skin temperature.
 163 α is the solubility of CO₂ at the respective subskin or skin temperature and salinities which was
 164 estimated as in Weiss (1974). $fCO_2_{(atm)}$ and $fCO_2_{(sw,subskin)}$ are the fugacity of CO₂ in the atmosphere
 165 and the seawater subskin layer respectively. Eq. 1 and the use of skin and subskin temperatures

166 accounts for vertical temperature gradients across the ocean's mass boundary layer as described in
167 Woolf et al. (2016), where we refer the reader for further information and the assignment of data to
168 the skin and subskin quantities is described below.

169 For the $f\text{CO}_2_{(sw,subskin)}$, we use complete $f\text{CO}_2_{(sw,subskin)}$ fields generated by an exemplar neural network
170 approach (University of Exeter Physics Feed Forward Neural Network with Uncertainties; UEP-FNN-
171 U) described in section 2.4. The CCI-SST and CMEMS SSS are considered representative of the
172 subskin temperature and salinities and used in the calculation of $\alpha_{subskin}$. For the atmospheric side, the
173 ocean's skin temperature was estimated from the CCI-SST with a cool skin deviation calculated with
174 NOAA-COARE3.5 (Bartreau Ludovic et al., 2021; Edson et al., 2013; Fairall et al., 1996) using
175 CCMP wind speed, CCI-SST and ERA5 fields (Hersbach et al., 2019) as inputs. Skin salinity was
176 calculated assuming a +0.1 psu change from the CMEMS SSS (i.e a salty skin) as in Watson et al.
177 (2020) and Woolf et al. (2019). $f\text{CO}_2_{(atm)}$ was calculated using NOAA-ERSL atmospheric dry mixing
178 ratio of CO_2 ($x\text{CO}_2_{(atm)}$), the skin temperature and ERA5 atmospheric pressure. Sea ice concentrations
179 from the OSISAF (OSI SAF, 2022) dataset were used for the ice component of Eq. 1.

180

181 **2.3. Air-sea CO_2 flux uncertainties**

182 The spatially and temporally varying air-sea CO_2 flux uncertainties were calculated using a
183 framework that assesses all identified sources of uncertainties (Figure 1). Figure 1 indicates the
184 sources of uncertainties that contribute to the individual components of Eq. 1. Uncertainties within
185 each component were propagated through the flux calculations using standard propagation techniques
186 (e.g., where a specific value is known) or a Monte Carlo uncertainty propagation approach (e.g.,
187 where the component is dependent upon input data), to produce an uncertainty in the air-sea CO_2 flux
188 due to each component (considered 95% confidence).

189 As an example, the process for propagating the uncertainties contributing to the K_{600} uncertainty are
190 described, where these principles apply to all components. K_{600} shows two sources of uncertainty: (1)
191 the gas transfer parameterisation uncertainty when parameterised with in situ observations, which has
192 been indicated as ~20% (Woolf et al., 2019) and (2) the uncertainty within the wind speed product
193 used in driving the gas transfer parameterisation. The first component can be propagated with
194 standard propagation techniques, resulting in a 20 % uncertainty (assumed to be 95 % confidence) in
195 the calculated CO_2 flux. The second wind speed uncertainty component was propagated through the
196 gas transfer parameterisation using a Monte Carlo uncertainty propagation, where the wind speed was
197 perturbed randomly 100 times within its uncertainty (0.9 ms^{-1} where we assume this was a 95%
198 confidence) (Mears et al., 2022a). The one standard deviation of the resulting distribution of K_{600} were
199 calculated, converted to a percentage uncertainty, and propagated using standard propagation
200 techniques to a CO_2 flux uncertainty. This resulted in a spatially varying uncertainty with a global

201 mean of ~20 %, however significantly varying regionally, ranging from 10 % to greater than 100 %.
 202 For a total uncertainty on K_{600} for each 1 degree region, the two components could be combined in
 203 quadrature assuming they are independent and uncorrelated (Taylor, 1997). This approach and
 204 principles apply to all components in Figure 1 except for the sea ice concentration and the
 205 interpolation of the fCO_2 data. The uncertainty estimate of the interpolated fCO_2 is a more specialised
 206 case which needs to capture multiple sources of uncertainty, which are the network uncertainty, input
 207 parameter uncertainties (of the inputs used for the interpolation) and the evaluation uncertainty, and
 208 the approach taken for this are given in the section 2.4.2. The sea ice uncertainty contribution was not
 209 included in the total air-sea CO_2 flux uncertainty due to the asymmetric nature of the sea ice
 210 concentration when applying a Monte Carlo uncertainty propagation (i.e the sea ice concentration
 211 cannot be less than 0 % or greater than 100 % and therefore the resulting uncertainty distribution after
 212 applying the Monte Carlo uncertainty propagation would become skewed). These asymmetric
 213 distributed uncertainties cannot be combined with the symmetric uncertainty distributions using
 214 standard propagation techniques (Taylor, 1997). Therefore the sea ice concentration uncertainties are
 215 assessed within the globally integrated uncertainties described in section 2.5.

216

217 **2.4. Calculating spatially complete fCO_2 (sw) data and estimating their uncertainties**

218 The sparse sampling of the in situ data used, the need to use an interpolation method, and the need for
 219 input data for the interpolation methods warrants a more comprehensive analysis of the fCO_2 data
 220 uncertainties. These sections now describe the interpolation technique and the approach for assessing
 221 the uncertainties for input into the framework in Figure 1.

222 **2.4.1 The neural network approach - University of Exeter physics feed forward neural** 223 **network with uncertainties (UEP-FNN-U)**

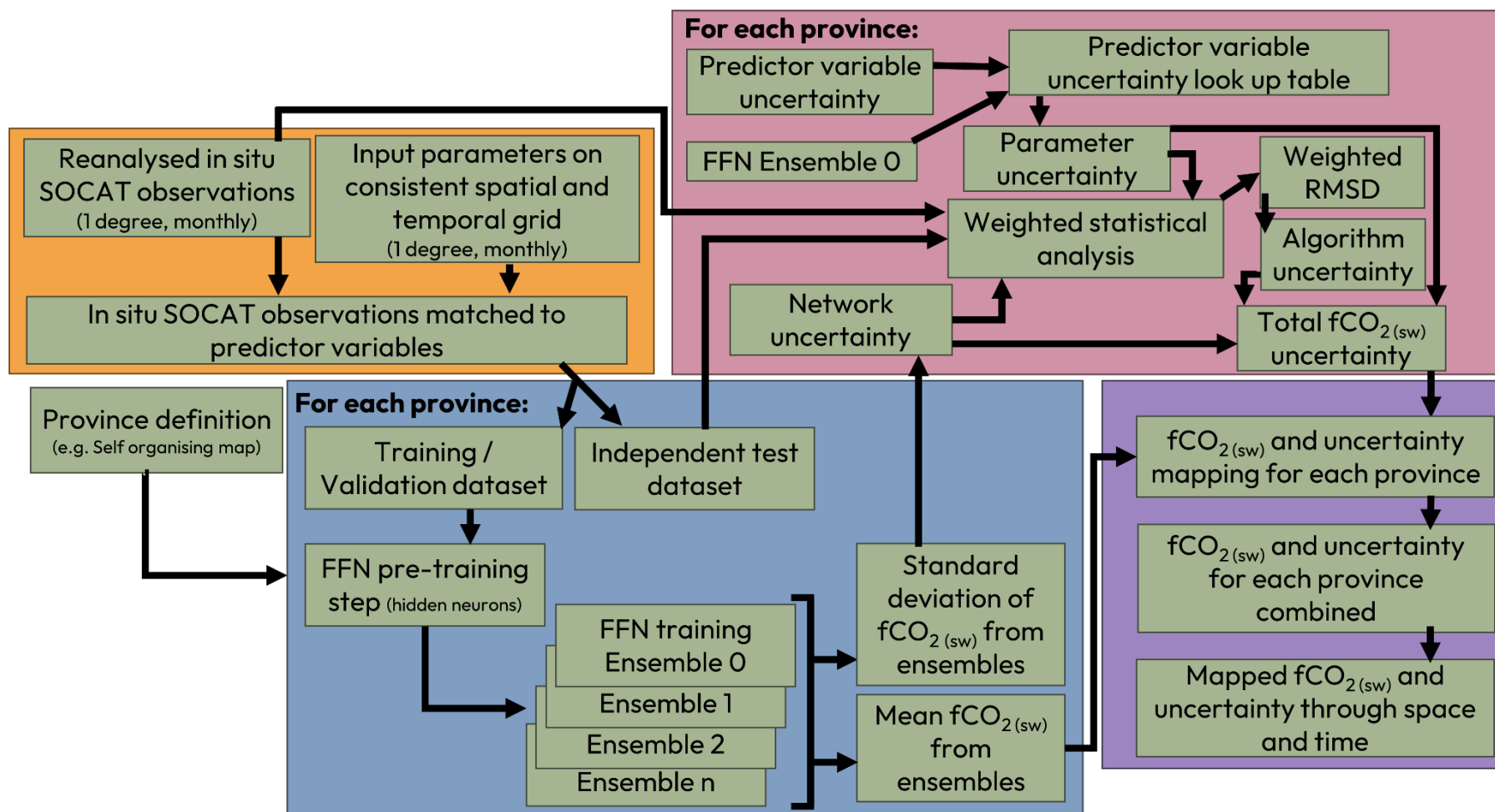
224 The self-organising map feed forward neural network (SOM-FNN) method (Landschützer et al., 2014,
 225 2016) used within the GCB (Friedlingstein et al., 2023) UoEx-Watson product (Watson et al., 2020)
 226 was applied with modifications to interpolate the re-analysed SOCAT sourced in situ fCO_2 data. These
 227 modification were: the Arctic Ocean was defined as a single province using the Longhurst province
 228 (Longhurst, 1998) Boreal Arctic (Province 1). The Mediterranean Sea and Red Sea Longhurst
 229 provinces (Province 16 and 25 respectively) were combined into a single province covering these
 230 regions, leading to a total of 18 provinces (instead of 17 as in UoEx-Watson) and near global
 231 coverage. Whereas the predictor variables remained consistent to the UoEx Watson product,
 232 consisting of SST, SSS, MLD, xCO_2 (atm), and anomalies of all four variables (Table 1).

233 These predictor variables were matched in space and time to the re-analysed SOCAT observations
 234 (Figure 2). For each province the SOCAT gridded fCO_2 (sw) observations, with their respective

235 predictor variables, were split into two datasets; (1) an independent test dataset that was not used in
 236 the neural network training or validation steps (5 %) and (2) a training and validation dataset (95 %).
 237 This data split provides as much of the data to the neural network training, whilst retaining a sufficient
 238 sample to independently assess the neural network performance. The training and validation dataset
 239 was then used within a feed forward neural network (FNN). The FNN approach consists of an input
 240 layer, hidden layer, and output layer. The input layer consists of nodes corresponding to the number of
 241 predictor variables, and a single node in the output layer. The number of nodes within the hidden layer
 242 was determined through a pre-training step (Ford et al., 2022a; Landschützer et al., 2014), which
 243 incrementally increases the hidden layer nodes in a set range (30 to 300 nodes at 30 increments) and
 244 finds the minimum of the neural network loss function which corresponds to the root mean square
 245 difference (RMSD) between the neural network output and the validation component training dataset.
 246 The pre-training step was required to provide the optimum number of hidden neurons to fit the in situ
 247 observations, whilst preventing overfitting (Demuth et al., 2008). Once the optimum number of nodes
 248 in the hidden layer was selected an ensemble of 10 neural networks are trained using the training and
 249 validation dataset. The training and validation dataset was split further and randomly into the training
 250 (70 %) and validation datasets (30 %) for each ensemble member. The split percentages were
 251 estimated with the optimal split approach described in Amari et al. (1997). This random splitting
 252 allows the neural network ensemble a high probability to see all the dataset as either training or
 253 validation data. Once all ensembles have been trained, the output $f\text{CO}_2(\text{sw})$ for the province was the
 254 mean of the ensembles. Applying this ‘mean’ neural network for each province to the complete fields
 255 of the predictor variables allows the generation of complete and spatially complete $f\text{CO}_2(\text{sw})$ fields
 256 (Figure 2).

257 **Table 1:** Input parameters used within the University of Exeter physics feed forward neural network
 258 (UEP-FNN-U) as predictor variables, with their respective uncertainties used within the parameter
 259 uncertainty.

Predictor Variables	Defined Uncertainty	Reference
NOAA $x\text{CO}_2(\text{atm})$	1 ppm	(Lan et al., 2023)
CCI Sea Surface Temperature (v2.1)	0.15 K	(Merchant et al., 2019)
CMEMS sea surface salinity (GLORYSV12)	0.1 psu	(Jean-Michel et al., 2021)
CMEMS mixed layer depth (GLORYSV12; \log_{10} transformed)	0.05 $\log_{10}(\text{m})$	(Jean-Michel et al., 2021)



260

261 **Figure 2:** Flowchart indicating the structure and training scheme of the feed forward neural network approach and uncertainty analysis as described within
 262 section 2.4.1 and 2.4.2. Acronyms in the flowchart are Surface ocean CO₂ Atlas (SOCAT), fugacity of CO₂ in seawater ($f\text{CO}_{2(\text{sw})}$), feed forward neural
 263 network (FFN) and root mean square difference (RMSD).

264 **2.4.2 Spatial and temporally varying $f\text{CO}_2$ (sw) uncertainty determination**

265 The characterisation of uncertainties in the $f\text{CO}_2$ (sw) neural network approach applied here allows the
266 determination of spatially and temporally varying uncertainties in the estimated $f\text{CO}_2$ (sw). Three
267 sources of uncertainty in the neural network $f\text{CO}_2$ (sw) are considered (and shown in Figure 2 in detail)
268 and these are analysed and then included within the air-sea CO_2 flux uncertainties framework within
269 Figure 1 (see the three boxes that are grouped by a dashed line in the bottom right of Figure 1).

270 The first uncertainty component consists of the neural network uncertainty, whereby the random
271 nature of the neural network approaches can lead to different optimum outcomes of a single network.
272 This uncertainty was assessed as two standard deviations (2σ) of 10 neural network ensemble runs
273 described in section 2.4.1 thereby providing the mean and standard deviation of the ensembles on a
274 per pixel basis. Regions where the 2σ value is small, indicates where the neural networks ensembles
275 are well constrained with different training and validation splits, and so output similar $f\text{CO}_2$ (sw)
276 estimates with low variability between estimates. The first ensemble member is also used within the
277 second uncertainty component of the $f\text{CO}_2$ (sw).

278 The second uncertainty component considered is the impact of the uncertainties in the predictor
279 variables on the resulting interpolated fields, as described in Ford et al. (2021), and applied to $f\text{CO}_2$ (sw)
280 in Ford et al. (2022a). The uncertainties in the predictor variables were propagated through the first
281 neural network ensemble (for practical reasons, this analysis was only applied to the first member of
282 the ensemble described above due to the computational load). In summary, a n-dimensional (n being
283 the number of predictor variables) linear spaced grid was constructed between the maximum and
284 minimum of each predictor variable. The linear spacing was determined such that the total number of
285 grid points does not exceed a defined value (whereby increasing this number increases the resolution
286 of the grid but increases computation). At each point in the grid, the predictor variables were
287 randomly perturbed within their uncertainty (Table 1; assuming these are 95% confidence) and the
288 $f\text{CO}_2$ (sw) estimated for each perturbation. The one standard deviation of the resulting $f\text{CO}_2$ (sw)
289 distribution was taken as the input parameter uncertainty. The process is repeated for every
290 combination in the n-dimensional grid. This grid became a look-up table for the input parameter
291 uncertainty on the $f\text{CO}_2$ (sw) using linear interpolation between grid points. Thus, allowing the
292 determination of the input parameter uncertainty at any combination of input variables, in a
293 computationally efficient setup.

294 The third uncertainty component considered was the evaluation uncertainty, or how accurate and
295 precise the neural network estimates of the $f\text{CO}_2$ (sw) are with respect to the in situ gridded SOCAT
296 observations. For each province the independent test observations are compared to the neural network
297 ensemble mean using a weighted statistical analysis as described in Ford et al. (2021). The weighting
298 procedure allows both uncertainties in the neural network and the in situ data to be included in the

299 assessment of the evaluation uncertainty. The neural network uncertainty for the weighting was
300 determined as the network and input parameter uncertainties combined in quadrature (Taylor, 1997),
301 consistent with Ford et al. (2021). The in situ observation uncertainty was calculated as the standard
302 deviation of the in situ SOCAT observations in a particular grid cell combined in quadrature with an
303 assumed measurement uncertainty of 5 μatm (Bakker et al., 2016; Taylor, 1997) (so information from
304 the two previously described uncertainty components are used within the derivation of this third
305 component). The weighted statistical analysis provides the bias (accuracy), root mean square
306 difference (RMSD; precision), along with the slope and intercept of a type II linear regression and the
307 number of observations. The neural network approaches generally have a bias (accuracy) near ~ 0
308 μatm indicating a high accuracy, however the RMSD (precision) is generally larger (values closer to
309 ~ 0 indicate a higher precision) (Ford et al., 2022a; Gregor et al., 2019; Landschützer et al., 2014). For
310 each province the weighted RMSD was taken as the combined algorithm uncertainty, and the bias
311 assumed to be negligible (i.e. maximum biases are $\sim 10\%$ of the corresponding RMSD) compared to
312 the RMSD (example per province scatter plots shown in Supplementary Figure S1).

313 Once all three components are calculated, these are combined in quadrature (Taylor, 1997) to provide
314 the total uncertainty on the $f\text{CO}_2(\text{sw})$. The three uncertainty components are all calculated or applied
315 during the mapping procedure to produce complete fields of $f\text{CO}_2(\text{sw})$ with a concurrent total
316 uncertainty (considered a 95% confidence uncertainty).

317

318 **2.5. Integrated air-sea CO_2 fluxes and uncertainties**

319 The monthly air-sea CO_2 fluxes and their uncertainties can be used to construct annual global budgets
320 of the net CO_2 flux. The area of each pixel was calculated assuming the Earth is an ellipsoid, and high
321 resolution land percentage masks were produced from The General Bathymetric Chart of the Oceans
322 (GEBCO) bathymetry data (GEBCO Bathymetric Compilation Group, 2023). The high resolution
323 approach ensures that coastal region contours are well captured to avoid unnecessary precision or
324 rounding errors (as described by Shutler et al., 2016). The calculated CO_2 fluxes ($\text{g C m}^{-2} \text{d}^{-1}$) are
325 multiplied by the pixel area (m^2), land percentage masks, the days within each month and then
326 summed into annual CO_2 fluxes (Pg C yr^{-1}). The annual absolute air-sea CO_2 flux was also calculated
327 (i.e. $|F|$, the absolute air-sea CO_2 flux from Eq 1, regardless of whether into or out of the ocean).

328 The integration of the air-sea CO_2 flux uncertainties within the uncertainty budget must be treated
329 carefully (Figure 1). In general most components within the air-sea CO_2 flux calculations have a
330 systematic component that will be correlated globally (Figure 1; blue boxes) and a component that
331 will be correlated to a spatial and temporal scale (Figure 1; green boxes). Following standard
332 geostatistical methods these two components (correlated globally and correlated to a spatial/temporal
333 scale) must be treated differently when integrating globally (see the Supplementary of Watson et al.,

334 2009). The globally correlated components (Figure 1; blue boxes) can be integrated in the same way
335 as the air-sea CO₂ fluxes. So the CO₂ flux uncertainty (g C m⁻² d⁻¹) at each pixel location was first
336 multiplied by the area of the pixel (m²), land percentage mask and the number of days in the month,
337 and then summed into an annual CO₂ flux uncertainty for each systematic component (Pg C yr⁻¹).
338 Whereas the procedure for globally integrating the uncertainty component that correlates to a spatial
339 and temporal scale (Figure 1; green boxes) requires an understanding of the scales at which spatial
340 features, and therefore their associated uncertainties, decorrelate. It was firstly assumed that the
341 uncertainties are not correlated between months (i.e no temporal correlation) as previous work shows
342 that for the SST (from the CCI-SST data) and sea ice concentrations (from the OSISAF data) the
343 uncertainties correlate up to period of only a few days (Kern, 2021). The spatial decorrelation length
344 for each component (Figure 1; green boxes) was assessed using a semi-variogram approach, as used
345 in previous studies (Landschützer et al., 2013, 2014; Watson et al., 2009). The analysis calculates the
346 semi-variance within the uncertainty field at point-to-point Haversine distances and estimates the
347 ‘range’, or the distance at which the semi-variance does not change. The range indicates the distance
348 within which the uncertainties can be deemed to be correlated.

349 The following methods are consistent with the variogram analysis used for air-sea CO₂ gas fluxes
350 within Watson et al. (2009) and Landschützer et al. (2013, 2014). The semi-variogram analysis was
351 implemented using SciKit-GStat v1.0 (Mälicke, 2022) parameterised with the Dowd semi-variance
352 estimator and fit to an exponential variogram model. The semi-variogram was fit to a random
353 subsample of 200 points extracted from each month’s uncertainty fields and repeated 100 times. The
354 monthly perturbations were combined into an annual distribution (~1200 perturbations) and the
355 median and interquartile range extracted from the distribution (example histograms for SST shown in
356 Supplementary Figure S2). In cases where a monthly uncertainty field had less than 200 points, the
357 subsample was constructed on the number of available points divided by two.

358 The uncertainty fields supplied to the semi variogram analysis fell into three categories: (1) a
359 complete uncertainty field, (2) incomplete fields of the residuals between the parameter and in situ
360 observations or (3) complete residual fields between two datasets for the parameter. The SST (CCI-
361 SST), and sea ice concentration (OSISAF) and fCO₂(_{sw}) network uncertainty (Figure 1) had full
362 uncertainty fields (category 1) which were applied to the semi variogram analysis indicating median
363 decorrelation lengths of ~1300 km, ~1500 km and ~1800 km respectively between 1985 and 2022.
364 Although complete uncertainty fields were available for fCO₂(_{sw}) parameter and evaluation, these
365 fields have non-continuous values resulting in a lack of convergence for the semi-variogram analysis
366 (i.e the methodological decisions in section 2.4.2 cause these fields to be roughly single values for
367 each province). Therefore for the fCO₂(_{sw}) evaluation and parameter uncertainties, we have to use an
368 incomplete uncertainty field (category 2 field) to estimate the decorrelation lengths. The residuals
369 between the in situ monthly SOCAT fCO₂(_{sw}) observations and the neural network ensemble mean are

370 mapped (category 2) and supplied to the semi-variogram approach. This gave a median decorrelation
371 length of ~2400 km. The wind speed uncertainty presents no complete uncertainty field or in situ
372 observations and therefore we assess the spatial residual variability between two differing wind speed
373 datasets, CCMP v3.1 and ERA5 wind speeds (category 3) as an estimate of the decorrelation lengths.
374 This analysis estimated a median decorrelation lengths of ~4000 km. Finally for $x\text{CO}_2(\text{atm})$ we assign a
375 decorrelation length of 2000 ± 1500 km estimated using the global locations of the in situ stations that
376 supply data to the NOAA-ERSL product, and for SSS we assume the uncertainty decorrelated at the
377 same spatial scale as the CCI-SST (~1300 km). The calculated decorrelation lengths varied in time
378 and had their respective uncertainties.

379 These decorrelation lengths have previously been used to estimate the number of decorrelated areas
380 within a region, either globally (Landschützer et al., 2014) or regionally (Landschützer et al., 2013;
381 Watson et al., 2009). The number of decorrelated regions are then combined with a spatially fixed
382 uncertainty to estimate the integrated uncertainty. However, in this study we have estimated spatially
383 varying uncertainty fields which cannot be applied to the methodology of the previous studies. We
384 therefore integrate the uncertainty component that correlates to a spatial scale using the calculated
385 decorrelation lengths and spatially varying uncertainty fields within a Monte Carlo uncertainty
386 propagation.

387 In summary, a global grid of points was calculated where each point was separated by twice the
388 decorrelation length for the component being calculated. At each point a random value between -1 and
389 1 was assigned. These values were then linearly interpolated onto the same 1 degree global grid as the
390 air-sea CO_2 flux data, such that each global 1 degree location has a value between -1 and 1 assigned.
391 This was repeated for each month in the timeseries between 1985 and 2022 producing a global grid of
392 perturbation values through time. This perturbation grid has systematic spatial structures (of values
393 between -1 and 1) that are consistent with the decorrelation length scale, and therefore the number of
394 decorrelated areas in previous studies (Landschützer et al., 2014; Watson et al., 2009). The complete
395 space time fields of the air-sea CO_2 flux uncertainty were multiplied by the perturbation values and
396 added to the calculated air-sea CO_2 flux. The annual net CO_2 flux budget calculations described at the
397 start of section 2.5 were conducted on the perturbed air-sea CO_2 fluxes. This process was repeated 100
398 times with the decorrelation length perturbed randomly within its uncertainty at the start of each
399 ensemble. The two standard deviations of the resulting 100 ensembles of annual net CO_2 fluxes were
400 taken as the globally integrated uncertainty of the component.

401 To provide confidence in our Monte Carlo uncertainty propagation methodology we replicate the
402 global integrated $f\text{CO}_2(\text{sw})$ uncertainty presented in Landschützer et al. (2014) of $\sim 0.18 \text{ Pg C yr}^{-1}$ (1σ)
403 for the period 1998 to 2010. Here we supply the calculated decorrelation lengths for the $f\text{CO}_2(\text{sw})$
404 evaluation uncertainty in this study, as our neural network approach is based on the Landschützer et

405 al. (2014) methodology, and a fixed $f\text{CO}_2(\text{sw})$ evaluation uncertainty of 12 μatm . With these inputs the
 406 Monte Carlo uncertainty propagation estimates a 1σ uncertainty of $\sim 0.17 \text{ Pg C yr}^{-1}$ for the period 1998
 407 to 2010, which is within 6% of, and consistent with, the Landschützer et al. (2014) result.

408 The integrated uncertainty components were calculated at the 95% confidence (or equivalent to a 2
 409 sigma uncertainty), but to enable comparisons to the GCB values (Friedlingstein et al., 2023) we also
 410 express these at 1 sigma.

411

412 **3. Results**

413 **3.1. $f\text{CO}_2(\text{sw})$ and $f\text{CO}_2(\text{sw})$ uncertainties**

414 The UEP-FNN-U estimated mean $f\text{CO}_2(\text{sw})$ between 1985 and 2022 showed global spatial variability
 415 consistent to the UoEx-Watson data product, but with extended coverage into the Arctic ocean and
 416 Mediterranean Sea (Supplementary Figure S3; Figure 3a). The concurrent mean total $f\text{CO}_2(\text{sw})$
 417 uncertainty estimated from the neural network showed a mean value of $\sim 30 \mu\text{atm}$, with clear
 418 geographical differences (Figure 3b). The subtropics generally showed lower uncertainties around ~ 20
 419 μatm , whereas larger uncertainties were prevalent in the Arctic Ocean, Southern Ocean and Equatorial
 420 Pacific with values greater than $40 \mu\text{atm}$.

421 The dominant component driving the total $f\text{CO}_2(\text{sw})$ uncertainty varied spatially (Figure 3 c,d,e). The
 422 $f\text{CO}_2(\text{sw})$ parameter uncertainty showed consistently lower values ranging from $2 \mu\text{atm}$ up to maxima
 423 at $\sim 10 \mu\text{atm}$ (Figure 3d). Maxima generally occurred in dynamic regions including the Arctic and
 424 Equatorial Pacific, however the parameter uncertainty was not a dominant source to the total
 425 uncertainty. The network uncertainty indicated minima around $\sim 10 \mu\text{atm}$ which occurred in the
 426 subtropics and increased to maxima greater than $\sim 50 \mu\text{atm}$ in the Arctic Ocean (Figure 3c). The
 427 evaluation uncertainty ranged from $\sim 10 \mu\text{atm}$ in the subtropics and Mediterranean Sea, up to maxima
 428 $\sim 40 \mu\text{atm}$ in the polar North Atlantic Ocean (Figure 3e). The evaluation uncertainty was generally the
 429 dominant component in the subtropics and the polar North Atlantic, whereas the network uncertainty
 430 was the dominant component in the Arctic Ocean and Equatorial Pacific. The network and evaluation
 431 uncertainties were both important components within the Southern Ocean (Figure 3c, e).

432

433 **3.2. Air-sea CO_2 flux uncertainties**

434 The mean total air-sea CO_2 flux uncertainties between 1985 and 2022 showed minima around $\sim 0.01 \text{ g}$
 435 $\text{C m}^{-2} \text{ d}^{-1}$ in the subtropics to maxima greater than $0.1 \text{ g C m}^{-2} \text{ d}^{-1}$ in the polar oceans (Figure 4a). In all
 436 regions, the total $f\text{CO}_2(\text{sw})$ uncertainty was the dominant component, with relative contributions
 437 ranging from 50 % to 75 % (Figure 4 b,c,d,e; Bar 0). In most regions, the next largest components to
 438 the uncertainty generally stemmed from the gas transfer parameterisation and the wind speed

439 uncertainties which is the dominant input to the gas transfer calculation (Figure 4 b,c,d,e; Bar 1). In
440 the Southern Ocean, the gas transfer parameterisation uncertainty was larger with relative
441 contributions greater than 50 %, compared to the wind speed uncertainty (Figure 4e; Bar 2). In the
442 polar North Atlantic, the gas transfer parameterisation and wind speed both contributed the same
443 (Figure 4c; Bar 2). However, in the subtropical South Atlantic and Equatorial Pacific the wind speed
444 uncertainty was larger than the gas transfer parameterisation component (Figure 4 a,d; Bar 2). The
445 remaining uncertainty components, including the $f\text{CO}_2(\text{atm})$, air and waterside solubilities and Schmidt
446 number, were generally smaller components with relative contributions totalling to around 5 % of the
447 total uncertainty (Figure 4 b,c,d; Bar 0). However in the Southern Ocean, the air and waterside
448 solubility components accounted for ~20 % of the total uncertainty and were larger than the gas
449 transfer and wind components (Figure 4e; Bar 0).

450

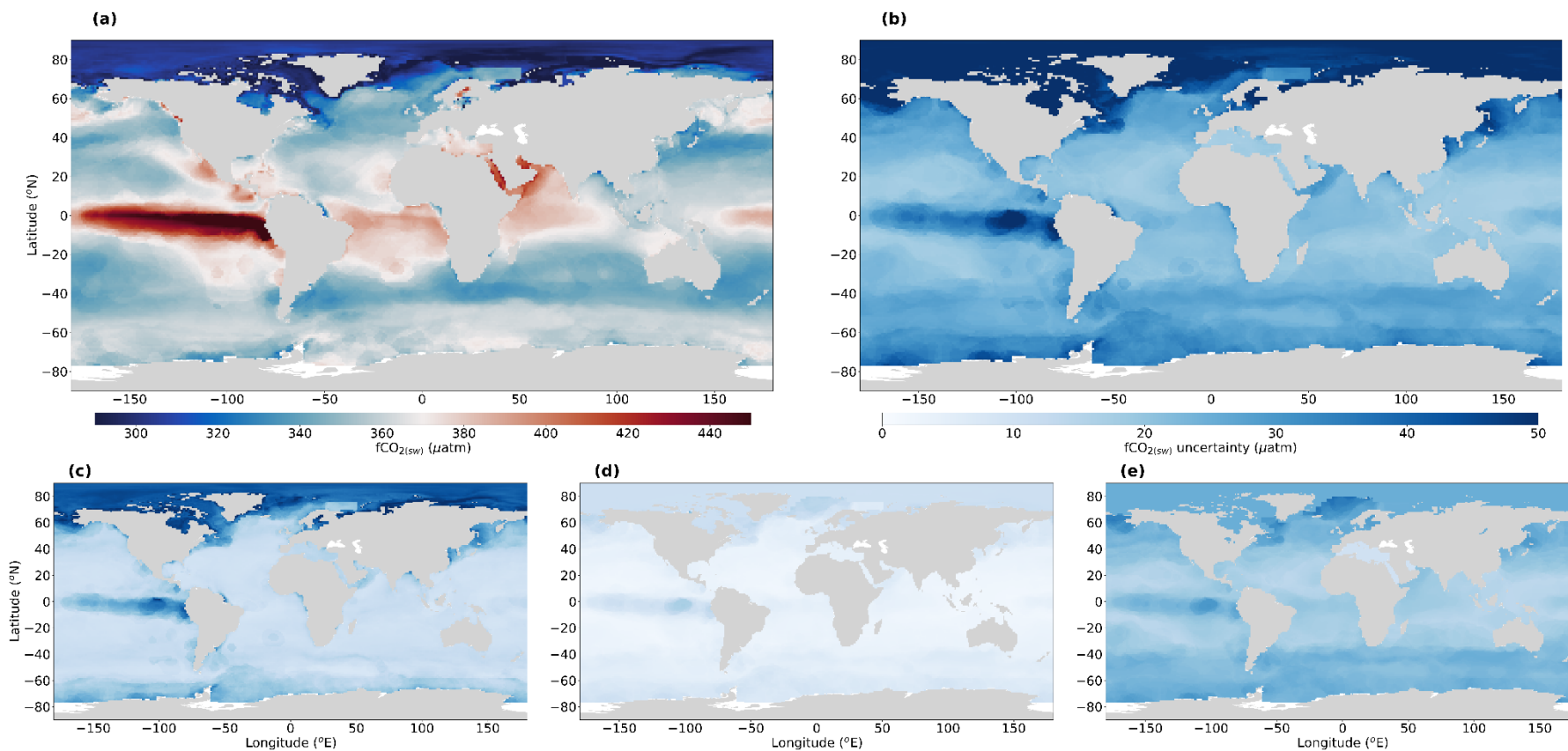
451 **3.3. Integrated net air-sea CO₂ flux and uncertainties**

452 The globally integrated net air-sea CO₂ flux indicated a net CO₂ sink of ~2.2 Pg C yr⁻¹ between 1985
453 to 1995 before reducing to a minimum in 2000 of ~2.0 Pg C yr⁻¹. There after the CO₂ sink increased
454 steadily from ~2.0 Pg C yr⁻¹ in 2002 to ~3.4 Pg C yr⁻¹ in 2020 (Figure 5d). The evolution of the CO₂
455 sink estimated by the UEP-FNN-U was consistent with that of the UoEx-Watson product (Figure 5d).
456 The one sigma total integrated CO₂ flux uncertainty had a mean of ~0.72 Pg C yr⁻¹ between 1985 and
457 2022, ranging from a minimum of ~0.60 Pg C yr⁻¹ around 2000 to a maximum of ~0.85 Pg C yr⁻¹ in
458 2021 (Figure 5d; Table 2).

459 The dominant components contributing to the total uncertainty changed over the period 1985 to 2022
460 (Figure 5a). Between 1985 and 2000, the $f\text{CO}_2(\text{sw})$ uncertainty decreased from ~0.65 Pg C yr⁻¹ to
461 ~0.45 Pg C yr⁻¹ but remained the dominant component in this period. During the period 2001 to 2022,
462 the $f\text{CO}_2(\text{sw})$ and gas transfer uncertainties show relatively equal contributions to the total uncertainty
463 of ~0.49 Pg C yr⁻¹. However after ~2010 the gas transfer uncertainties were marginally more
464 dominant. The $f\text{CO}_2(\text{sw})$ uncertainty was made up by the three sources of neural network uncertainty
465 (Figure 5b). The parameter uncertainty showed the lowest contribution of ~10 %, whereas the
466 evaluation and network uncertainties have contributions of 50 % and 40 % respectively. But these
467 contributions changed through time, whereby the evaluation uncertainty contribution were generally
468 higher at the start and end of the timeseries, with minima around 1997. The network uncertainty
469 showed a reciprocal change to that of the evaluation uncertainty, whereas the parameter uncertainty
470 stayed relatively constant through time.

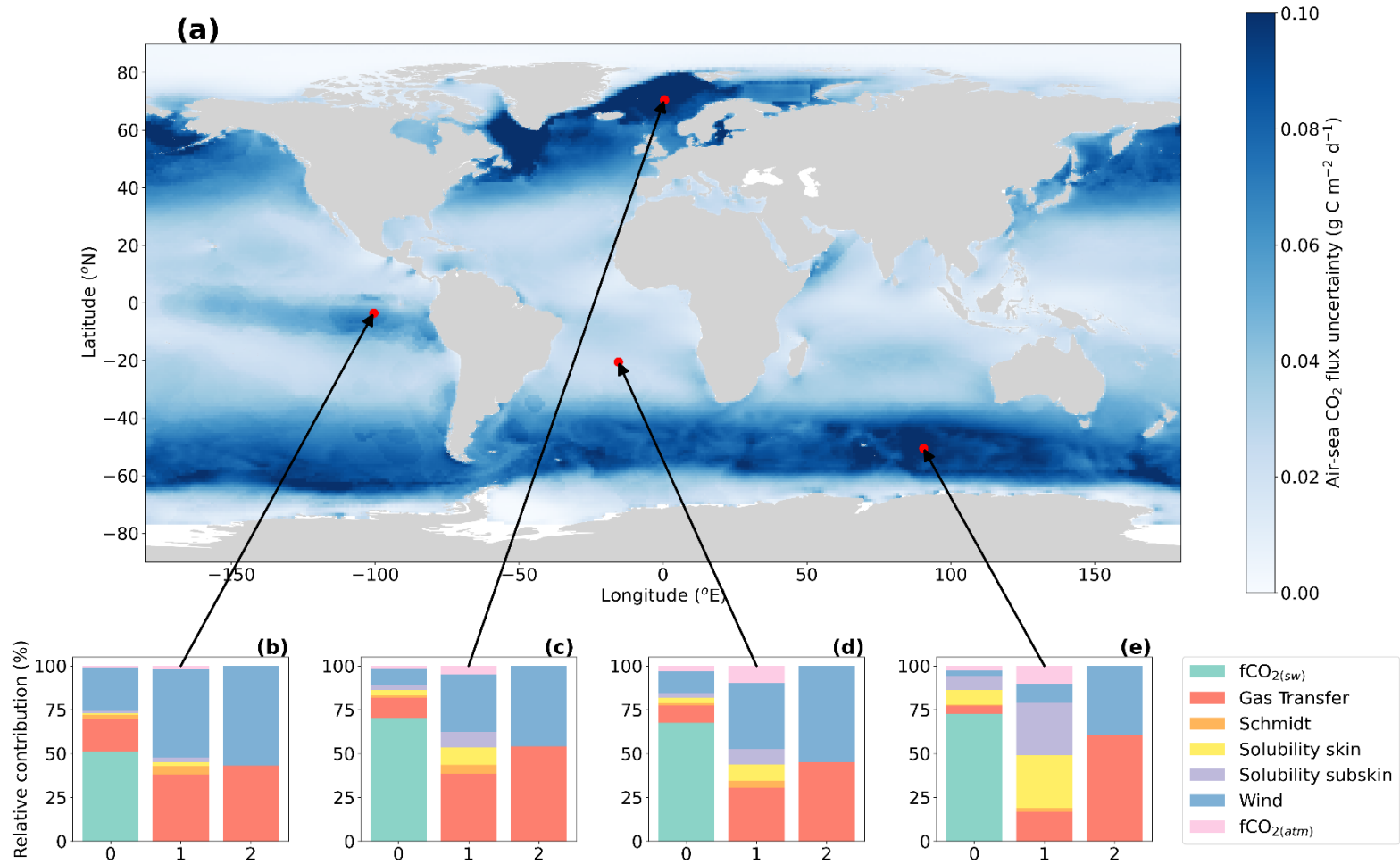
471 The gas transfer parameterisation uncertainty was the next dominant component of uncertainty after
472 the $f\text{CO}_2(\text{sw})$, increasing from 0.40 Pg C yr⁻¹ in 1985 to 0.58 Pg C yr⁻¹ in 2022. This increase largely
473 followed the increase in the absolute air-sea CO₂ flux, from 4 Pg C yr⁻¹ in 1985 to 5.8 Pg C yr⁻¹ in

474 2022 (Figure 5d). After ~2010 the gas transfer parameterisation became the marginally more
475 dominant source of uncertainty, and before this period the $f\text{CO}_{2(\text{sw})}$ remained the dominant source of
476 uncertainty. The other components showed lower contributions to the total uncertainty with mean
477 contributions between 1985 and 2022 of $0.14 \text{ Pg C yr}^{-1}$ for the wind speed, $0.08 \text{ Pg C yr}^{-1}$ for the
478 solubility components, $0.06 \text{ Pg C yr}^{-1}$ for the Schmidt number, $0.02 \text{ Pg C yr}^{-1}$ for the $f\text{CO}_{2(\text{atm})}$ and
479 $0.003 \text{ Pg C yr}^{-1}$ for the sea ice uncertainty. The $f\text{CO}_{2(\text{atm})}$ component was dominated by the $x\text{CO}_{2(\text{atm})}$
480 uncertainty and contained a 25 % relative contribution from the partial pressure of water vapour
481 (pH_2O) component used in the calculation (Figure 5c). These components showed small increases
482 following the increase in the absolute air-sea CO_2 flux (Figure 5d).



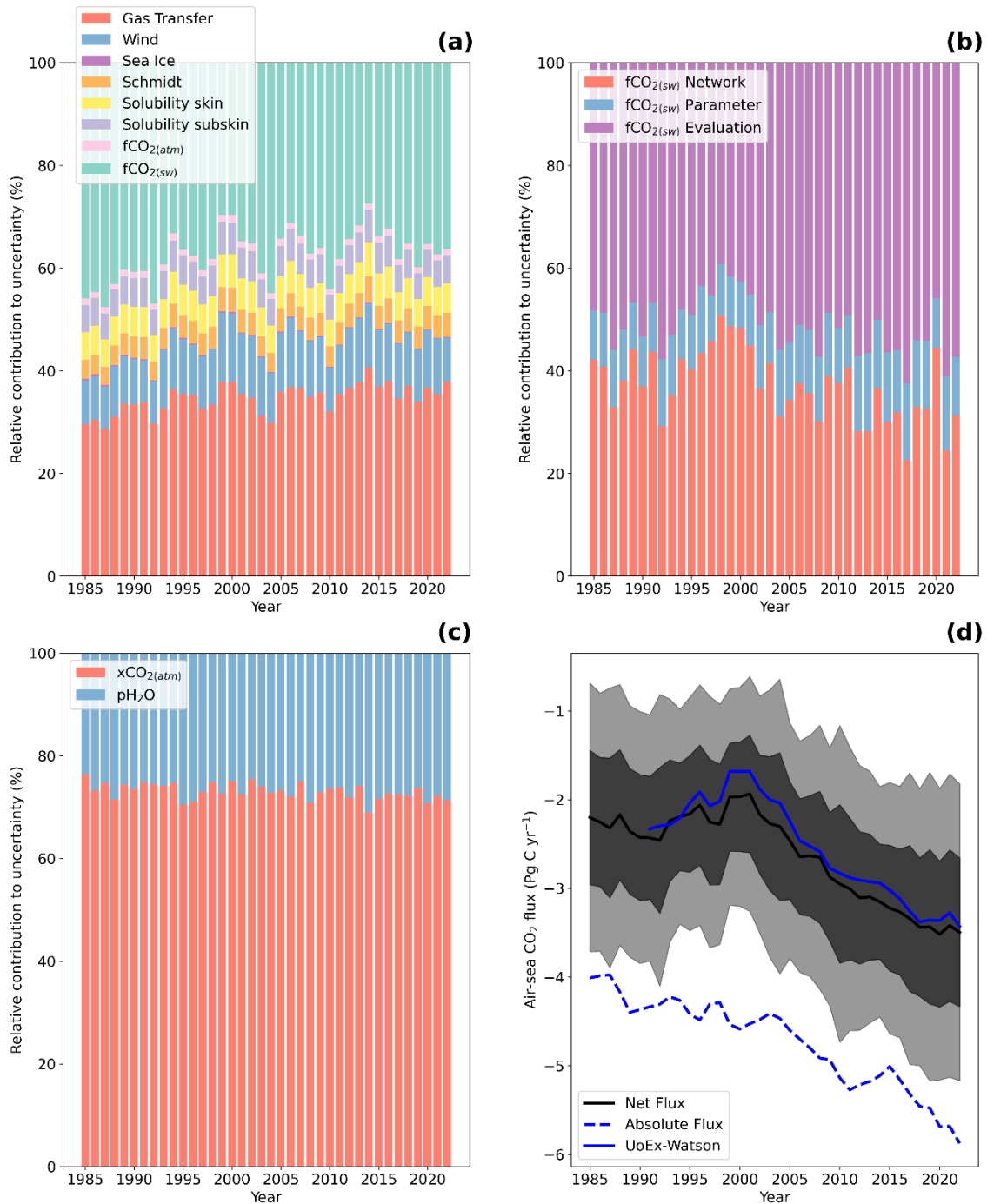
483

484 **Figure 3:** (a) Global mean fCO₂(sw) between 1985 and 2022 where the colorbar is centred on the mean atmospheric CO₂ concentration for the same period. (b)
 485 Global mean total fCO₂(sw) uncertainty between 1985 and 2022. (c) same as (b) but for the fCO₂(sw) network uncertainty. (d) same as (b) but for the fCO₂(sw)
 486 parameter uncertainty. (e) same as (b) but for the fCO₂(sw) evaluation uncertainty. Note (c), (d) and (e) are plotted on the same colorbar as (b).



487

488 **Figure 4:** (a) Global mean air-sea CO₂ flux uncertainty between 1985 and 2022. (b) Mean relative contribution bar chart for each of the air-sea CO₂ flux
 489 uncertainty components between 1985 and 2022 at the highlighted location. Bar 0 shows all labelled sources of uncertainty. Bar 1 shows the contributions for
 490 all components removing the fCO_{2(sw)} component. Bar 2 shows the relative contribution for the wind speed and gas transfer components. (c), (d) and (e) same
 491 as (b) but for the respective points highlighted.



492

493 **Figure 5:** (a) Mean relative contributions between 1985 to 2022 for each uncertainty component to
 494 the globally integrated air-sea CO₂ flux. (b) Same as (a) but for the three fCO_{2(sw)} uncertainty
 495 components that contribute to the total fCO_{2(sw)} in (a). (c) same as (b) but for the two uncertainty
 496 components that contribute to the fCO_{2(atm)} in (a). (d) Net air-sea CO₂ flux calculated between 1985
 497 and 2022 (black line). Dark grey region indicates the one sigma, and light grey region indicates the
 498 two sigma total air-sea CO₂ flux uncertainty. Blue dashed line indicates the absolute air-sea CO₂ flux
 499 (i.e the integrated absolute CO₂ flux across the air-sea interface). Blue line indicates the UoEx-Watson
 500 product from the Global Carbon Budget 2023 (Friedlingstein et al., 2023).

501 **Table 2:** Mean 1σ uncertainty between 1985 to 2022 for each component. These mean uncertainty can
 502 be split into a fixed (globally correlated) component and a component that was correlated to a spatial
 503 and temporal period. The total mean uncertainty between 1985 and 2022 assuming the uncertainties
 504 are independent and uncorrelated (Taylor, 1997) is shown in the total row. Equivalent 2σ uncertainties
 505 shown in Supplementary Table S2.

Component	Mean 1σ uncertainty between 1985 to 2022 (Pg C yr ⁻¹)	Mean fixed component contribution (Pg C yr ⁻¹)	Mean spatially varying component (Pg C yr ⁻¹)
Gas transfer	0.47	0.47	N/A
Wind	0.14	N/A	0.14
Sea ice	0.003	N/A	0.003
Schmidt	0.06	0.06	0.001
Solubility skin	0.08	0.08	0.02
Solubility subskin	0.07	0.07	0.02
fCO ₂ (atm)	0.02	0.005	0.02
fCO ₂ (sw)	0.51	N/A	0.51
Total	0.72		

506

507 4. Discussion

508 4.1. Air-sea CO₂ flux and fCO₂ (sw) uncertainties

509 Within this study, we present an air-sea CO₂ flux uncertainty budget that builds on the principles of in
 510 situ Fiducial Reference Measurement (Banks et al., 2020) where all known sources of uncertainty are
 511 systematically considered (however small) and propagated to the final uncertainty using standard
 512 propagation techniques and a well-established uncertainty framework (BIPM, 2008; Taylor, 1997).
 513 Applying this approach has allowed the production of spatially and temporally complete air-sea CO₂
 514 flux uncertainties. We showed in all cases that the fCO₂ (sw) uncertainties were the dominant source of
 515 uncertainty to the air-sea CO₂ flux when investigating individual locations and time points. This
 516 would indicate that when assessing variability or trends in the air-sea CO₂ fluxes, as a first step the
 517 fCO₂ (sw) uncertainty should be accounted for within these assessments. For example, Ford et al.
 518 (2022b) calculated trends in the air-sea CO₂ fluxes in the South Atlantic Ocean and showed significant
 519 trends whilst accounting for the fCO₂ (sw) and gas transfer uncertainties. However, in this study in the
 520 South Atlantic Ocean the wind speed uncertainty component was larger than the gas transfer
 521 uncertainty (Figure 4e), consistent with the results of Jersild and Landschützer (2024). Similarly in the
 522 Southern Ocean, the air and waterside solubility component were larger than both the gas transfer and
 523 wind speed uncertainties (Figure 4e). Therefore, it is important to assess all sources of uncertainties
 524 within the air-sea CO₂ fluxes as some components may be more dominant in some regions as opposed

525 to others (Figure 4). These uncertainties should also be considered when assessing trends and/or more
526 complex decompositions of seasonal, interannual and decadal variability (Ford et al., 2022b;
527 Landschützer et al., 2016, 2018). A concerted effort to implement these full uncertainty budgets for
528 the air-sea CO₂ fluxes in preparation for future advances and reductions of uncertainties in the air-sea
529 CO₂ flux calculations would appear critical.

530 Within this air-sea CO₂ flux uncertainty budget, a spatially and temporally explicit approach to
531 estimating the total fCO_{2(sw)} uncertainty from an exemplar feed forward neural network approach
532 (Landschützer et al., 2014; Watson et al., 2020) was implemented (named UEP-FNN-U). Previous
533 fCO_{2(sw)} uncertainty estimates have assumed a fixed global value based on a comparison to the in situ
534 SOCAT observations (Landschützer et al., 2013, 2014) which is equivalent to the evaluation
535 uncertainty in this study. Our results show that in the subtropics the use of the single fixed evaluation
536 uncertainty may be applicable, as this was the dominant uncertainty within these regions. However,
537 within more dynamic regions, such as the Arctic Ocean and Equatorial Pacific, the evaluation
538 uncertainty will likely underestimate the total uncertainty due to the dominance of the network
539 uncertainty within these regions. Some regional approaches have started to incorporate these further
540 sources of uncertainty into their total fCO_{2(sw)} uncertainty (Ford et al., 2022a). Therefore, these results
541 would indicate a need to expand the current uncertainty estimation for globally resolved fCO_{2(sw)},
542 using the approach in this study as a framework.

543 Within the GCB multiple data-products produce globally complete fCO_{2(sw)} fields, which use different
544 interpolation methodologies (Friedlingstein et al., 2023). These methods include neural networks
545 (Chau et al., 2022; Landschützer et al., 2014; Watson et al., 2020), multi-linear regression (Iida et al.,
546 2021) or other machine learning techniques (Gloege et al., 2022), and therefore the basis of the three
547 uncertainty components to the fCO_{2(sw)} in this study can be adapted to equivalent uncertainties for
548 these methodologies. For example, for a method that uses multi-linear regression e.g. (Iida et al.,
549 2021) instead of a feed-forward neural network, the calculation of the evaluation uncertainty (i.e
550 comparison to the in situ SOCAT observations) would remain the same. The network uncertainty
551 could be formed from either the standard deviation of multiple ensemble runs of the multi-linear
552 regression (similar to the network uncertainty in this study) or could be constructed from the
553 uncertainty in the linear regression fit parameters as the source of uncertainty. The parameter
554 uncertainty would be similar to the approach in this study and would involve a Monte Carlo
555 uncertainty propagation which propagates the input parameter uncertainties through the multi-linear
556 regression. It is therefore clear that these uncertainties could be equivalently mapped by data-products
557 to produce spatially and temporally complete fCO_{2(sw)} uncertainty fields in future releases. This would
558 be important as clearly the complete fCO_{2(sw)} uncertainty fields form a key component in calculating
559 spatially and temporally complete air-sea CO₂ flux.

560

561 **4.2. Integrated air-sea CO₂ flux uncertainties**

562 Within the GCB the ocean carbon sink has been assessed by annually integrating the calculated air-
563 sea CO₂ fluxes. The uncertainty on these estimates is assessed using literature values, and not all
564 sources of uncertainty are evaluated within the assessment. In this study we have systematically
565 assessed the components that contribute to the total air-sea CO₂ flux uncertainty and showed that
566 these vary through time (Figure 5a, d). In this section we discuss the uncertainty estimates for the
567 different components and compare these to the current GCB uncertainty estimate.

568 The GCB estimate for the fCO_{2(sw)} mapping uncertainty is 0.20 Pg C yr⁻¹, compared to the 0.51 Pg C
569 yr⁻¹ (Table 2) uncertainty identified in this study. The GCB estimate stems from Landschützer et al.
570 (2014) where the uncertainty was estimated using the evaluation uncertainty of ~12 µatm. As an
571 example, applying a 12 µatm evaluation uncertainty, and assuming the network and parameter
572 uncertainties are 0, our methodology produces a mean 0.17 Pg C yr⁻¹ uncertainty due to the fCO_{2(sw)}
573 between 1998 and 2010 (same period as Landschützer et al., 2014) so our calculation methods are
574 consistent with that of the earlier Landschützer et al. (2014) work. Since the initial work by
575 Landschützer et al. (2014), the evaluation uncertainty for most data products has increased to around
576 ~20 µatm (22 µatm for the UEP-FNN-U; Supplementary Figure S3c) (Gregor et al., 2019). This
577 increase in the evaluation uncertainty increases the fCO_{2(sw)} evaluation uncertainty to a mean of 0.41
578 Pg C yr⁻¹ between 1985 and 2022, but within this study we also consider the network (0.29 Pg C yr⁻¹)
579 and parameter uncertainties (0.09 Pg C yr⁻¹). These three components all contribute to the larger
580 uncertainty of 0.51 Pg C yr⁻¹ than that estimated by Landschützer et al. (2014).

581 The gas transfer uncertainty has been assessed at 0.20 Pg C yr⁻¹ within the GCB, compared to the 0.47
582 Pg C yr⁻¹ (Table 2) in this study. Woolf et al. (2019) suggest two representative values for the gas
583 transfer uncertainty of 0.20 Pg C yr⁻¹ (1 sigma assuming a 10 % gas transfer uncertainty) or 0.40 Pg C
584 yr⁻¹ (1 sigma assuming a 20 % gas transfer uncertainty). In this study we estimate a slightly higher
585 uncertainty than suggested by Woolf et al. (2019), however our results indicate that this uncertainty
586 was proportional to the absolute air-sea CO₂ flux (Figure 5d) which is feasible given the potential bias
587 introduced by bubbles and increasing atmospheric CO₂ concentrations (Leighton et al., 2018).

588 Although our result was higher than the current GCB estimate it remains consistent if the 10 % gas
589 transfer uncertainty were selected. However, we propose the use of the 20 % uncertainty as a
590 conservative estimate for the gas transfer uncertainty, and that this component be calculated for each
591 product based on the absolute air-sea CO₂ flux.

592 Recently the evaluation of wind speed products has indicated that a 0.09 Pg C yr⁻¹ (Fay et al., 2021;
593 Roobaert et al., 2018) uncertainty stems from the wind speed uncertainty. We have shown a slightly

594 larger but still consistent value of $0.14 \text{ Pg C yr}^{-1}$ (Table 2) using a different methodology. Fay et al.
 595 (2021) estimate the uncertainty as the standard deviation of the net CO_2 sink calculated using three
 596 different wind products, where the standard deviation may not, with a small sample size, represent the
 597 full uncertainty within the wind products. Our results may also be slightly larger due to the connection
 598 to the absolute air-sea CO_2 flux, which is likely different from the products used within the previous
 599 work.

600 The other components assessed in this study have not previously been investigated and are currently
 601 not included within the GCB estimates. The solubility components within this study introduce a 0.08
 602 Pg C yr^{-1} uncertainty. The inclusion of two solubility terms within this study stems from the inclusion
 603 of vertical temperature gradients at the ocean's surface, as described in Woolf et al. (2016). The skin
 604 and subskin solubilities are calculated at slightly different temperatures and salinities (cool and salty
 605 skin), and therefore have subtly different values when integrated globally. Within the GCB, all the
 606 data-product based assessments, except for the UoEx-Watson, do not include the vertical temperature
 607 gradients (Friedlingstein et al., 2023) and therefore have a single solubility term. Although the
 608 evidence is growing for the inclusion of these temperature gradients (Bellenger et al., 2023; Dong et
 609 al., 2022; Shutler et al., 2020; Watson et al., 2020; Woolf et al., 2016), the use of a single or two
 610 solubilities does not have a large effect on the uncertainty (i.e. $0.10 \text{ Pg C yr}^{-1}$ for two solubilities, or
 611 $0.08 \text{ Pg C yr}^{-1}$ for one solubility assuming the solubilities are independent and uncorrelated).

612 The sea ice component presents a very small uncertainty on the global scale of $0.003 \text{ Pg C yr}^{-1}$. The
 613 inclusion of sea ice within the air-sea CO_2 flux calculation assumes the flux decreases linearly within
 614 increasing sea ice concentration (i.e. ice is a complete barrier to air-sea fluxes) (Arrigo & Van Dijken,
 615 2007; Shutler et al., 2016; Takahashi et al., 2009). Although there remains debate within sea ice
 616 communities as to the relationship between sea ice coverage and air-sea CO_2 fluxes. This is in part
 617 due conflicting observations that fluxes can occur through sea ice (e.g. Geilfus et al., 2014) and
 618 whether sea ice inhibits (e.g. Prytherch & Yelland, 2021) or enhances (e.g. Kohout & Meylan, 2008)
 619 turbulence, thereby modifying the CO_2 flux (see discussion and references within Watts et al., 2022).
 620 These components will introduce further uncertainties into the sea ice component but cannot currently
 621 be quantified. However, at the global scale these uncertainties will remain small relative to the other
 622 components due to the small areal coverage but will likely increase on regional scales.

623 We have focussed our uncertainty analysis on the global scale, however the principles and
 624 calculations applied globally are applicable to the regional scale. Within regional assessments the
 625 fixed components will remain of similar relative magnitudes. However, the spatially correlated
 626 components will increase in magnitude due to the calculated decorrelation lengths (i.e. as the region
 627 assessed gets smaller, the uncertainties within the region become more correlated and therefore larger
 628 when integrated). Previous GCB assessments have shown global agreement between the data-product

629 based approaches within the uncertainties (Friedlingstein et al., 2022, 2023) but regional differences
630 are still relatively large e.g. (Fay & McKinley, 2021; Ford et al., 2022a; Friedlingstein et al., 2023). In
631 future work, the application of the uncertainty framework in this study to regional air-sea CO₂ flux
632 budgets will be an important step to improve future regional air-sea CO₂ flux budgets.

633

634 **4.3. Uncertainty estimates for the Global Carbon Budget**

635 The GCB has identified that the data-products and models which assess the global ocean carbon sink
636 have been slowly diverging, and are starting to diverge outside the current calculated uncertainty (see
637 Figure 10 in Friedlingstein et al., 2023). Hauck, Nissen et al. (2023) indicated the ocean carbon sink
638 uncertainty for the data products may be underestimated and suggested a value of 0.6 Pg C yr⁻¹ before
639 the riverine adjustment uncertainty was included. Within this study we show an updated mean
640 uncertainty of 0.72 Pg C yr⁻¹ between 1985 and 2022, before the riverine adjustment and in situ fCO₂
641 _(sw) uncertainty were included. When the in situ fCO₂ _(sw) uncertainty of 0.2 Pg C yr⁻¹ (which can be
642 calculated within the approach assuming a 2 µatm fCO₂ _(sw) uncertainty that is correlated globally;
643 (Bakker et al., 2016)) and river flux adjustment uncertainty of 0.15 Pg C yr⁻¹ (0.3 Pg C yr⁻¹ is the 2
644 sigma equivalent uncertainty (Regnier et al., 2022)) are included, assuming these are independent and
645 uncorrelated we estimate a GCB equivalent mean uncertainty for the UEP-FNN-U of 0.76 Pg C yr⁻¹.
646 Although we have calculated a fixed value here which could be used within future GCB assessments,
647 we strongly recommend that each data product be assessed to determine their own uncertainty budgets
648 and then a full and temporally varying uncertainty budget for the GCB data-product ensemble can be
649 derived. Our results have shown that the size and dominance of the different components vary through
650 time, and some components show variability that follows the absolute air-sea CO₂ flux which will be
651 different for each product and will likely track atmospheric emissions. This study could be used as a
652 framework to allow these uncertainties to be calculated for each data product for future releases of the
653 GCB assessments. All software for the analysis framework and the gas flux calculations are available
654 as open-source (CC-BY licence) and these are version controlled and fully traceable (Ford et al.,
655 2024).

656

657 **5. Conclusions**

658 In this study, we have presented a framework to estimate spatially and temporally varying air-sea CO₂
659 flux uncertainties, which systematically assessed all sources of uncertainties and was built upon
660 standard uncertainty propagation methodologies and an established uncertainty approach. We show
661 when investigating single locations the fCO₂ _(sw) was the dominant source of uncertainty to the air-sea
662 CO₂ fluxes. However, we show the relative contributions by the remaining sources of uncertainty

663 varied spatially, such that the gas transfer uncertainty was not always the second most dominant
664 source of uncertainty. The $f\text{CO}_2(\text{sw})$ uncertainties were estimated using a similar systematic uncertainty
665 budget that considered three sources of uncertainties in an exemplar feed forward neural network
666 scheme (the UEP-FNN-U). We show that the evaluation uncertainty (comparison to SOCAT in situ
667 observations) was the largest source of uncertainty in the subtropics, however the network uncertainty
668 (uncertainty within the neural network ensemble) was dominant in dynamic regions such as the Arctic
669 Ocean. The parameter uncertainty (propagated input parameter uncertainties through the neural
670 network) was a small contribution to the combined uncertainty.

671 The calculated air-sea CO_2 fluxes were integrated into an annual estimates of the net air-sea CO_2 flux,
672 or the ocean carbon sink, between 1985 to 2022 as commonly produced for the Global Carbon Budget
673 assessments. We present an approach to integrate the calculated air-sea CO_2 flux uncertainties
674 providing temporally varying ocean carbon sink uncertainties. We showed a mean 1 sigma ocean
675 carbon sink uncertainty between 1985 and 2022 of $0.72 \text{ Pg C yr}^{-1}$. Over this period, the $f\text{CO}_2(\text{sw})$
676 component equated to a mean of $0.51 \text{ Pg C yr}^{-1}$, followed by the gas transfer at $0.47 \text{ Pg C yr}^{-1}$. The
677 dominant component switched from the $f\text{CO}_2(\text{sw})$ before ~ 2010 , to the gas transfer after ~ 2010 .
678 Smaller sources of uncertainty included the wind speed uncertainty ($0.14 \text{ Pg C yr}^{-1}$), solubility (0.08
679 Pg C yr^{-1}) and Schmidt number ($0.06 \text{ Pg C yr}^{-1}$).

680 Finally we provide a Global Carbon Budget equivalent mean 1 sigma uncertainty (i.e including the
681 riverine flux adjustment and in situ $f\text{CO}_2(\text{sw})$ uncertainties) of $0.76 \text{ Pg C yr}^{-1}$ for the UEP-FNN-U. This
682 study provides an approach to estimating a complete air-sea CO_2 flux uncertainty budget, that could
683 be used by the community to provide time varying and consistent uncertainties for use within the
684 Global Carbon Budget and other assessment studies.

685

686 **Contributions (CRediT)**

687 Daniel J. Ford: Conceptualization, Formal Analysis, Investigation, Methodology, Software,
688 Validation, Visualization, Writing-original draft

689 Josh Blannin: Methodology, Software, Writing-review and editing.

690 Jennifer Watts: Conceptualisation, Writing-review and editing

691 Andrew Watson: Conceptualisation, Writing-review and editing, Project Administration, Funding
692 acquisition

693 Peter Landschützer: Conceptualisation, Software, Writing-review and editing

694 Annika Jersild: Conceptualisation, Writing-review and editing

695 Jamie D. Shutler: Conceptualisation, Formal Analysis, Methodology, Writing-review and editing,
696 Project Administration, Funding acquisition, Supervision
697

698 **Open research statement**

699 Input datasets used within this study are tabulated in Supplementary Table S1 with their respective
700 DOIs. The software used within this study is available open source at Ford et al. (2024), and updated
701 at <https://github.com/JamieLab/OceanICU>. Output from the analysis in this study, including the input
702 datasets on the 1 degree monthly grid, output from the UEP-FNN-U, air-sea CO₂ fluxes and their
703 respective uncertainty components can be downloaded from Ford et al. (in prep for Zenodo).

704

705 **Acknowledgements**

706 This work was funded by the Convex Seascape Survey (<https://convexseascapesurvey.com/>) and the
707 European Union under grant agreement no. 101083922 (OceanICU; <https://ocean-icu.eu/>) and UK
708 Research and Innovation (UKRI) under the UK government's Horizon Europe funding guarantee
709 [grant number 10054454, 10063673, 10064020, 10059241, 10079684, 10059012, 10048179]. The
710 views, opinions and practices used to produce this dataset/software are however those of the author(s)
711 only and do not necessarily reflect those of the European Union or European Research Executive
712 Agency. Neither the European Union nor the granting authority can be held responsible for them.

713 The Surface Ocean CO₂ Atlas (SOCAT) is an international effort, endorsed by the International Ocean
714 Carbon Coordination Project (IOCCP), the Surface Ocean Lower Atmosphere Study (SOLAS) and the
715 Integrated Marine Biosphere Research (IMBeR) program, to deliver a uniformly quality-controlled
716 surface ocean CO₂ database. The many researchers and funding agencies responsible for the collection
717 of data and quality control are thanked for their contributions to SOCAT.

718

719 **References**

- 720 Amari, S. I., Murata, N., Müller, K. R., Finke, M., & Yang, H. H. (1997). Asymptotic statistical theory
721 of overtraining and cross-validation. *IEEE Transactions on Neural Networks*, 8(5), 985–996.
722 <https://doi.org/10.1109/72.623200>
- 723 Arrigo, K. R., & Van Dijken, G. L. (2007). Interannual variation in air-sea CO₂ flux in the Ross Sea,
724 Antarctica: A model analysis. *Journal of Geophysical Research: Oceans*, 112(C3),
725 2006JC003492. <https://doi.org/10.1029/2006JC003492>

- 726 Bakker, D. C. E., Pfeil, B., Landa, C. S., Metzl, N., O'Brien, K. M., Olsen, A., et al. (2016). A multi-
727 decade record of high-quality fCO₂ data in version 3 of the Surface Ocean CO₂ Atlas
728 (SOCAT). *Earth System Science Data*, 8(2), 383–413. [https://doi.org/10.5194/essd-8-383-](https://doi.org/10.5194/essd-8-383-2016)
729 2016
- 730 Banks, A. C., Vendt, R., Alikas, K., Bialek, A., Kuusk, J., Lerebourg, C., et al. (2020). Fiducial
731 reference measurements for satellite ocean colour (FRM4SOC). *Remote Sensing*, 12(8).
732 <https://doi.org/10.3390/RS12081322>
- 733 Bariteau Ludovic, Blomquist Byron, Fairall Christopher, Thompson Elizabeth, Jim, E., & Pincus
734 Robert. (2021, July 16). Python implementation of the COARE 3.5 Bulk Air-Sea Flux
735 algorithm (Version v1.1). Zenodo. <https://doi.org/10.5281/ZENODO.5110991>
- 736 Bellenger, H., Bopp, L., Ethé, C., Ho, D., Duvel, J. P., Flavoni, S., et al. (2023). Sensitivity of the
737 Global Ocean Carbon Sink to the Ocean Skin in a Climate Model. *Journal of Geophysical*
738 *Research: Oceans*, 128(7), e2022JC019479. <https://doi.org/10.1029/2022JC019479>
- 739 BIPM. (2008). *Evaluation of measurement data—Guide to the expression of uncertainty in*
740 *measurement*.
- 741 Chau, T. T. T., Gehlen, M., & Chevallier, F. (2022). A seamless ensemble-based reconstruction of
742 surface ocean CO₂ and air–sea CO₂ fluxes over the global coastal and open oceans.
743 *Biogeosciences*, 19(4), 1087–1109. <https://doi.org/10.5194/bg-19-1087-2022>
- 744 Demuth, H., Beale, M., & Hagan, M. (2008). *Neural Network Toolbox 6 Users Guide*. The
745 *MathWorks, Inc.* 3 Apple Hill Drive, Natick, MA.
- 746 Dong, Y., Yang, M., Bakker, D. C. E., Kitidis, V., & Bell, T. G. (2021). Uncertainties in eddy
747 covariance air–sea CO₂ flux measurements and implications for gas transfer velocity
748 parameterisations. *Atmospheric Chemistry and Physics*, 21(10), 8089–8110.
749 <https://doi.org/10.5194/acp-21-8089-2021>
- 750 Dong, Y., Bakker, D. C. E., Bell, T. G., Huang, B., Landschützer, P., Liss, P. S., & Yang, M. (2022).
751 Update on the Temperature Corrections of Global Air-Sea CO₂ Flux Estimates. *Global*
752 *Biogeochemical Cycles*, 36(9). <https://doi.org/10.1029/2022GB007360>

- 753 Edson, J. B., Jampana, V., Weller, R. A., Bigorre, S. P., Plueddemann, A. J., Fairall, C. W., et al.
754 (2013). On the Exchange of Momentum over the Open Ocean. *Journal of Physical*
755 *Oceanography*, 43(8), 1589–1610. <https://doi.org/10.1175/JPO-D-12-0173.1>
- 756 Fairall, C. W., Bradley, E. F., Godfrey, J. S., Wick, G. A., Edson, J. B., & Young, G. S. (1996). Cool-
757 skin and warm-layer effects on sea surface temperature. *Journal of Geophysical Research:*
758 *Oceans*, 101(C1), 1295–1308. <https://doi.org/10.1029/95JC03190>
- 759 Fay, A. R., & McKinley, G. A. (2021). Observed Regional Fluxes to Constrain Modeled Estimates of
760 the Ocean Carbon Sink. *Geophysical Research Letters*, 48(20), e2021GL095325.
761 <https://doi.org/10.1029/2021GL095325>
- 762 Fay, A. R., Gregor, L., Landschützer, P., McKinley, G. A., Gruber, N., Gehlen, M., et al. (2021).
763 SeaFlux: harmonization of air–sea CO₂ fluxes from surface CO₂ data products using a
764 standardized approach. *Earth System Science Data*, 13(10), 4693–4710.
765 <https://doi.org/10.5194/essd-13-4693-2021>
- 766 Ford, D. J., Tilstone, G. H., Shutler, J. D., Kitidis, V., Lobanova, P., Schwarz, J., et al. (2021). Wind
767 speed and mesoscale features drive net autotrophy in the South Atlantic Ocean. *Remote*
768 *Sensing of Environment*, 260, 112435. <https://doi.org/10.1016/j.rse.2021.112435>
- 769 Ford, D. J., Tilstone, G. H., Shutler, J. D., & Kitidis, V. (2022a). Derivation of seawater pCO₂ from
770 net community production identifies the South Atlantic Ocean as a CO₂ source.
771 *Biogeosciences*, 19(1), 93–115. <https://doi.org/10.5194/bg-19-93-2022>
- 772 Ford, D. J., Tilstone, G. H., Shutler, J. D., & Kitidis, V. (2022b). Identifying the biological control of
773 the annual and multi-year variations in South Atlantic air–sea CO₂ flux. *Biogeosciences*,
774 19(17), 4287–4304. <https://doi.org/10.5194/bg-19-4287-2022>
- 775 Ford, D. J., Sims, R. P., Shutler, J. D., Ashton, I., & Holding, T. (2023). Reanalysed (depth and
776 temperature consistent) surface ocean CO₂ atlas (SOCAT) version 2023 (Version 2023-0)
777 [Data set]. Zenodo. <https://doi.org/10.5281/ZENODO.8229316>
- 778 Ford, D. J., Blannin, J., Watts, J., Watson, A. J., Landschützer, P., Jersild, A., & Shutler, J. D. (2024).
779 OceanICU Neural Network Framework with per pixel uncertainty propagation (Version
780 v1.0.0). [Software]. <https://doi.org/10.5281/ZENODO.10868001>

- 781 Friedlingstein, P., O’Sullivan, M., Jones, M. W., Andrew, R. M., Gregor, L., Hauck, J., et al. (2022).
782 Global Carbon Budget 2022. *Earth System Science Data*, *14*(11), 4811–4900.
783 <https://doi.org/10.5194/essd-14-4811-2022>
- 784 Friedlingstein, P., O’Sullivan, M., Jones, M. W., Andrew, R. M., Bakker, D. C. E., Hauck, J., et al.
785 (2023). Global Carbon Budget 2023. *Earth System Science Data*, *15*(12), 5301–5369.
786 <https://doi.org/10.5194/essd-15-5301-2023>
- 787 GEBCO Bathymetric Compilation Group. (2023). The GEBCO_2023 Grid - a continuous terrain
788 model of the global oceans and land. (Version 1) [Documents, Network Common Data Form].
789 NERC EDS British Oceanographic Data Centre NOC. [https://doi.org/10.5285/F98B053B-](https://doi.org/10.5285/F98B053B-0CBC-6C23-E053-6C86ABC0AF7B)
790 [0CBC-6C23-E053-6C86ABC0AF7B](https://doi.org/10.5285/F98B053B-0CBC-6C23-E053-6C86ABC0AF7B)
- 791 Geilfus, N.-X., Tison, J.-L., Ackley, S. F., Galley, R. J., Rysgaard, S., Miller, L. A., & Delille, B.
792 (2014). Sea ice CO₂ dynamics and air–ice CO₂ fluxes during the Sea Ice Mass Balance in the
793 Antarctic (SIMBA) experiment – Bellingshausen Sea, Antarctica. *The Cryosphere*, *8*(6),
794 2395–2407. <https://doi.org/10.5194/tc-8-2395-2014>
- 795 Gloege, L., Yan, M., Zheng, T., & McKinley, G. A. (2022). Improved Quantification of Ocean Carbon
796 Uptake by Using Machine Learning to Merge Global Models and pCO₂ Data. *Journal of*
797 *Advances in Modeling Earth Systems*, *14*(2), e2021MS002620.
798 <https://doi.org/10.1029/2021MS002620>
- 799 Gregor, L., & Gruber, N. (2021). OceanSODA-ETHZ: a global gridded data set of the surface ocean
800 carbonate system for seasonal to decadal studies of ocean acidification. *Earth System Science*
801 *Data*, *13*(2), 777–808. <https://doi.org/10.5194/essd-13-777-2021>
- 802 Gregor, L., Lebehot, A. D., Kok, S., & Scheel Monteiro, P. M. (2019). A comparative assessment of
803 the uncertainties of global surface ocean CO₂ estimates using a machine-learning ensemble
804 (CSIR-ML6 version 2019a)-Have we hit the wall? *Geoscientific Model Development*, *12*(12),
805 5113–5136. <https://doi.org/10.5194/gmd-12-5113-2019>
- 806 Hauck, J., Landschützer, P., Mayot, N., & Jersild, A. (2023). Global Carbon Budget 2023, surface
807 ocean fugacity of CO₂ (fCO₂) and air-sea CO₂ flux of individual global ocean biogeochemical

- 808 models and surface ocean fCO₂-based data-products [Data set]. Zenodo.
809 <https://doi.org/10.5281/ZENODO.10222484>
- 810 Hauck, J., Nissen, C., Landschützer, P., Rödenbeck, C., Bushinsky, S., & Olsen, A. (2023). Sparse
811 observations induce large biases in estimates of the global ocean CO₂ sink: an ocean model
812 subsampling experiment. *Philosophical Transactions of the Royal Society A: Mathematical,*
813 *Physical and Engineering Sciences*, 381(2249), 20220063.
814 <https://doi.org/10.1098/rsta.2022.0063>
- 815 Hersbach, H., Bell, B., Berrisford, P., Biavati, G., Horányi, A., Muñoz Sabater, J., Nicolas, J., et al.
816 (2019). ERA5 monthly averaged data on single levels from 1979 to present. *Copernicus*
817 *Climate Change Service (C3S) Climate Data Store (CDS) [Dataset]*.
818 <https://doi.org/10.24381/cds.f17050d7>
- 819 Ho, D. T., Wanninkhof, R., Schlosser, P., Ullman, D. S., Hebert, D., & Sullivan, K. F. (2011). Toward
820 a universal relationship between wind speed and gas exchange: Gas transfer velocities
821 measured with ³He/SF₆ during the Southern Ocean Gas Exchange Experiment. *Journal of*
822 *Geophysical Research*, 116, C00F04. <https://doi.org/10.1029/2010JC006854>
- 823 Holding, T., Ashton, I. G., Shutler, J. D., Land, P. E., Nightingale, P. D., Rees, A. P., et al. (2019). The
824 FluxEngine air–sea gas flux toolbox: simplified interface and extensions for in situ analyses
825 and multiple sparingly soluble gases. *Ocean Science*, 15(6), 1707–1728.
826 <https://doi.org/10.5194/os-15-1707-2019>
- 827 Iida, Y., Takatani, Y., Kojima, A., & Ishii, M. (2021). Global trends of ocean CO₂ sink and ocean
828 acidification: an observation-based reconstruction of surface ocean inorganic carbon
829 variables. *Journal of Oceanography*, 77(2), 323–358. [https://doi.org/10.1007/s10872-020-](https://doi.org/10.1007/s10872-020-00571-5)
830 [00571-5](https://doi.org/10.1007/s10872-020-00571-5)
- 831 Jean-Michel, L., Eric, G., Romain, B.-B., Gilles, G., Angélique, M., Marie, D., et al. (2021). The
832 Copernicus Global 1/12° Oceanic and Sea Ice GLORYS12 Reanalysis. *Frontiers in Earth*
833 *Science*, 9(July), 1–27. <https://doi.org/10.3389/feart.2021.698876>

- 834 Jersild, A., & Landschützer, P. (2024). A Spatially Explicit Uncertainty Analysis of the Air-Sea CO₂
835 Flux From Observations. *Geophysical Research Letters*, *51*(4), e2023GL106636.
836 <https://doi.org/10.1029/2023GL106636>
- 837 Kern, S. (2021). Spatial Correlation Length Scales of Sea-Ice Concentration Errors for High-
838 Concentration Pack Ice. *Remote Sensing*, *13*(21), 4421. <https://doi.org/10.3390/rs13214421>
- 839 Kohout, A. L., & Meylan, M. H. (2008). An elastic plate model for wave attenuation and ice floe
840 breaking in the marginal ice zone. *Journal of Geophysical Research: Oceans*, *113*(C9),
841 2007JC004434. <https://doi.org/10.1029/2007JC004434>
- 842 Lan, X., Tans, P., Thoning, K., & NOAA Global Monitoring Laboratory. (2023). NOAA Greenhouse
843 Gas Marine Boundary Layer Reference - CO₂. [Data set]. NOAA GML.
844 <https://doi.org/10.15138/DVNP-F961>
- 845 Landschützer, P., Gruber, N., Bakker, D. C. E., Schuster, U., Nakaoka, S., Payne, M. R., et al. (2013).
846 A neural network-based estimate of the seasonal to inter-annual variability of the Atlantic
847 Ocean carbon sink. *Biogeosciences*, *10*(11), 7793–7815. [https://doi.org/10.5194/bg-10-7793-](https://doi.org/10.5194/bg-10-7793-2013)
848 2013
- 849 Landschützer, P., Gruber, N., Bakker, D. C. E., & Schuster, U. (2014). Recent variability of the global
850 ocean carbon sink. *Global Biogeochemical Cycles*, *28*(9), 927–949.
851 <https://doi.org/10.1002/2014GB004853>
- 852 Landschützer, P., Gruber, N., & Bakker, D. C. E. (2016). Decadal variations and trends of the global
853 ocean carbon sink. *Global Biogeochemical Cycles*, *30*(10), 1396–1417.
854 <https://doi.org/10.1002/2015GB005359>
- 855 Landschützer, P., Gruber, N., Bakker, D. C. E., Stemmler, I., & Six, K. D. (2018). Strengthening
856 seasonal marine CO₂ variations due to increasing atmospheric CO₂. *Nature Climate Change*,
857 *8*(2), 146–150. <https://doi.org/10.1038/s41558-017-0057-x>
- 858 Leighton, T. G., Coles, D. G. H., Srokosz, M., White, P. R., & Woolf, D. K. (2018). Asymmetric
859 transfer of CO₂ across a broken sea surface. *Scientific Reports*, *8*(1), 8301.
860 <https://doi.org/10.1038/s41598-018-25818-6>
- 861 Longhurst, A. (1998). *Ecological geography of the sea*. San Diego: Academic Press.

- 862 Mälicke, M. (2022). SciKit-GStat 1.0: a SciPy-flavored geostatistical variogram estimation toolbox
863 written in Python. *Geoscientific Model Development*, *15*(6), 2505–2532.
864 <https://doi.org/10.5194/gmd-15-2505-2022>
- 865 Mears, C., Lee, T., Ricciardulli, L., Wang, X., & Wentz, F. (2022a). Improving the Accuracy of the
866 Cross-Calibrated Multi-Platform (CCMP) Ocean Vector Winds. *Remote Sensing*, *14*(17),
867 4230. <https://doi.org/10.3390/rs14174230>
- 868 Mears, C., Lee, T., Ricciardulli, L., Wang, X., & Wentz, F. (2022b). RSS Cross-Calibrated Multi-
869 Platform (CCMP) monthly ocean vector wind analysis on 0.25 deg grid, Version 3.0 [Data
870 set]. <https://doi.org/10.56236/RSS-uv1m30>
- 871 Merchant, C. J., Embury, O., Bulgin, C. E., Block, T., Corlett, G. K., Fiedler, E., et al. (2019).
872 Satellite-based time-series of sea-surface temperature since 1981 for climate applications.
873 *Scientific Data*, *6*(1), 223. <https://doi.org/10.1038/s41597-019-0236-x>
- 874 Nightingale, P. D., Malin, G., Law, C. S., Watson, A. J., Liss, P. S., Liddicoat, M. I., et al. (2000). In
875 situ evaluation of air-sea gas exchange parameterizations using novel conservative and
876 volatile tracers. *Global Biogeochemical Cycles*, *14*(1), 373–387.
877 <https://doi.org/10.1029/1999GB900091>
- 878 OSI SAF. (2022). GBL SICO CDR R3Global Sea Ice Concentration Climate Data Record v3.0 -
879 Multimission (Version 3) [netCDF4]. OSI SAF.
880 https://doi.org/10.15770/EUM_SAF_OSI_0013
- 881 Prytherch, J., & Yelland, M. J. (2021). Wind, Convection and Fetch Dependence of Gas Transfer
882 Velocity in an Arctic Sea-Ice Lead Determined From Eddy Covariance CO₂ Flux
883 Measurements. *Global Biogeochemical Cycles*, *35*(2), e2020GB006633.
884 <https://doi.org/10.1029/2020GB006633>
- 885 Regnier, P., Resplandy, L., Najjar, R. G., & Ciais, P. (2022). The land-to-ocean loops of the global
886 carbon cycle. *Nature*, *603*(7901), 401–410. <https://doi.org/10.1038/s41586-021-04339-9>
- 887 Roobaert, A., Laruelle, G. G., Landschützer, P., & Regnier, P. (2018). Uncertainty in the global
888 oceanic CO₂ uptake induced by wind forcing: quantification and spatial analysis.
889 *Biogeosciences*, *15*(6), 1701–1720. <https://doi.org/10.5194/bg-15-1701-2018>

- 890 Shutler, J. D., Land, P. E., Piolle, J. F., Woolf, D. K., Goddijn-Murphy, L., Paul, F., et al. (2016).
891 FluxEngine: A flexible processing system for calculating atmosphere-ocean carbon dioxide
892 gas fluxes and climatologies. *Journal of Atmospheric and Oceanic Technology*, 33(4), 741–
893 756. <https://doi.org/10.1175/JTECH-D-14-00204.1>
- 894 Shutler, J. D., Wanninkhof, R., Nightingale, P. D., Woolf, D. K., Bakker, D. C., Watson, A., et al.
895 (2020). Satellites will address critical science priorities for quantifying ocean carbon.
896 *Frontiers in Ecology and the Environment*, 18(1), 27–35. <https://doi.org/10.1002/fee.2129>
- 897 Shutler, J. D., Gruber, N., Findlay, H. S., Land, P. E., Gregor, L., Holding, T., et al. (2024). The
898 increasing importance of satellite observations to assess the ocean carbon sink and ocean
899 acidification. *Earth-Science Reviews*, 250, 104682.
900 <https://doi.org/10.1016/j.earscirev.2024.104682>
- 901 Takahashi, T., Sutherland, S. C., Wanninkhof, R., Sweeney, C., Feely, R. A., Chipman, D. W., et al.
902 (2009). Climatological mean and decadal change in surface ocean pCO₂, and net sea-air CO₂
903 flux over the global oceans. *Deep-Sea Research Part II: Topical Studies in Oceanography*,
904 56(8–10), 554–577. <https://doi.org/10.1016/j.dsr2.2008.12.009>
- 905 Taylor, J. R. (1997). *An introduction to error analysis*. Sausalito, Calif.: University Science Books.
- 906 Wanninkhof, R. (2014). Relationship between wind speed and gas exchange over the ocean revisited.
907 *Limnology and Oceanography: Methods*, 12(JUN), 351–362.
908 <https://doi.org/10.4319/lom.2014.12.351>
- 909 Wanninkhof, R., Park, G. H., Takahashi, T., Sweeney, C., Feely, R., Nojiri, Y., et al. (2013). Global
910 ocean carbon uptake: Magnitude, variability and trends. *Biogeosciences*, 10(3), 1983–2000.
911 <https://doi.org/10.5194/bg-10-1983-2013>
- 912 Watson, A. J., Schuster, U., Bakker, D. C. E., Bates, N. R., Corbière, A., González-Dávila, M., et al.
913 (2009). Tracking the Variable North Atlantic Sink for Atmospheric CO₂. *Science*, 326(5958),
914 1391–1393. <https://doi.org/10.1126/science.1177394>
- 915 Watson, A. J., Schuster, U., Shutler, J. D., Holding, T., Ashton, I. G. C., Landschützer, P., et al. (2020).
916 Revised estimates of ocean-atmosphere CO₂ flux are consistent with ocean carbon inventory.
917 *Nature Communications*, 11(1), 1–6. <https://doi.org/10.1038/s41467-020-18203-3>

- 918 Watts, J., Bell, T. G., Anderson, K., Butterworth, B. J., Miller, S., Else, B., & Shutler, J. (2022).
919 Impact of sea ice on air-sea CO₂ exchange – A critical review of polar eddy covariance
920 studies. *Progress in Oceanography*, 201, 102741.
921 <https://doi.org/10.1016/j.pocean.2022.102741>
- 922 Weiss, R. F. (1974). Carbon dioxide in water and seawater: the solubility of a non-ideal gas. *Marine*
923 *Chemistry*, 2(3), 203–215. [https://doi.org/10.1016/0304-4203\(74\)90015-2](https://doi.org/10.1016/0304-4203(74)90015-2)
- 924 Weiss, R. F., & Price, B. A. (1980). Nitrous oxide solubility in water and seawater. *Marine Chemistry*,
925 8(4), 347–359. [https://doi.org/10.1016/0304-4203\(80\)90024-9](https://doi.org/10.1016/0304-4203(80)90024-9)
- 926 Woolf, D. K., Land, P. E., Shutler, J. D., Goddijn-Murphy, L. M., & Donlon, C. J. (2016). On the
927 calculation of air-sea fluxes of CO₂ in the presence of temperature and salinity gradients.
928 *Journal of Geophysical Research: Oceans*, 121(2), 1229–1248.
929 <https://doi.org/10.1002/2015JC011427>
- 930 Woolf, D. K., Shutler, J. D., Goddijn-Murphy, L., Watson, A. J., Chapron, B., Nightingale, P. D., et al.
931 (2019). Key Uncertainties in the Recent Air-Sea Flux of CO₂. *Global Biogeochemical Cycles*,
932 33(12), 1548–1563. <https://doi.org/10.1029/2018GB006041>

933

934 **References from Supporting Information**

- 935 CMEMS. (2021). Copernicus Marine Modelling Service global ocean physics reanalysis product
936 (GLORYS12V1). Copernicus Marine Modelling Service [Data Set]. [https://doi.org/10.48670/moi-](https://doi.org/10.48670/moi-00021)
937 00021
- 938 Ford, D. J., Sims, R. P., Shutler, J. D., Ashton, I., & Holding, T. (2023). Reanalysed (depth and
939 temperature consistent) surface ocean CO₂ atlas (SOCAT) version 2023 (Version 2023-0) [Data set].
940 Zenodo. <https://doi.org/10.5281/ZENODO.8229316>
- 941 Hauck, J., Landschützer, P., Mayot, N., & Jersild, A. (2023). Global Carbon Budget 2023, surface
942 ocean fugacity of CO₂ (fCO₂) and air-sea CO₂ flux of individual global ocean biogeochemical models
943 and surface ocean fCO₂-based data-products [Data set]. Zenodo.
944 <https://doi.org/10.5281/ZENODO.10222484>
- 945 Hersbach, H., Bell, B., Berrisford, P., Biavati, G., Horányi, A., Muñoz Sabater, J., Nicolas, J., et al.
946 (2019). ERA5 monthly averaged data on single levels from 1979 to present. Copernicus Climate
947 Change Service (C3S) Climate Data Store (CDS) [Dataset]. <https://doi.org/10.24381/cds.fl7050d7>

- 948 Jean-Michel, L., Eric, G., Romain, B.-B., Gilles, G., Angélique, M., Marie, D., et al. (2021). The
949 Copernicus Global 1/12° Oceanic and Sea Ice GLORYS12 Reanalysis. *Frontiers in Earth Science*,
950 9(July), 1–27. <https://doi.org/10.3389/feart.2021.698876>
- 951 Lan, X., Tans, P., Thoning, K., & NOAA Global Monitoring Laboratory. (2023). NOAA Greenhouse
952 Gas Marine Boundary Layer Reference - CO₂. [Data set]. NOAA GML.
953 <https://doi.org/10.15138/DVNP-F961>
- 954 Mears, C., Lee, T., Ricciardulli, L., Wang, X., & Wentz, F. (2022a). Improving the Accuracy of the
955 Cross-Calibrated Multi-Platform (CCMP) Ocean Vector Winds. *Remote Sensing*, 14(17), 4230.
956 <https://doi.org/10.3390/rs14174230>
- 957 Mears, C., Lee, T., Ricciardulli, L., Wang, X., & Wentz, F. (2022b). RSS Cross-Calibrated Multi-
958 Platform (CCMP) monthly ocean vector wind analysis on 0.25 deg grid, Version 3.0 [Data set].
959 <https://doi.org/10.56236/RSS-uv1m30>
- 960 Merchant, C. J., Embury, O., Bulgin, C. E., Block, T., Corlett, G. K., Fiedler, E., et al. (2019).
961 Satellite-based time-series of sea-surface temperature since 1981 for climate applications. *Scientific*
962 *Data*, 6(1), 223. <https://doi.org/10.1038/s41597-019-0236-x>
- 963 Taylor, J. R. (1997). *An introduction to error analysis*. Sausalito, Calif.: University Science Books.
- 964